Journal of Instrumentation

PAPER • OPEN ACCESS

Performance of the electromagnetic and hadronic prototype segments of the ALICE Forward Calorimeter

To cite this article: M. Aehle *et al* 2024 *JINST* **19** P07006

PUBLISHED BY IOP PUBLISHING FOR SISSA MEDIALAB

RECEIVED: *March 18, 2024*
ACCEPTED: *June 10, 2024*
PUBLISHED: *July 5, 2024*

Performance of the electromagnetic and hadronic prototype segments of the ALICE Forward Calorimeter

M. Aehle,[a] J. Alme,[b] C. Arata,[c] I. Arsene,[d] I. Bearden,[e] T. Bodova,[b] V. Borshchov,[f] O. Bourrion,[c] M. Bregant,[g] A. van den Brink,[h] V. Buchakchiev,[i] A. Buhl,[e] T. Chujo,[j,*] L. Dufke,[e] V. Eikeland,[b] M. Fasel,[k] N. Gauger,[a] A. Gautam,[l] A. Ghimouz,[j] Y. Goto,[m] R. Guernane,[c] T. Hachiya,[n] H. Hassan,[o] L. He,[p] H. Helstrup,[q] L. Huhta,[o] M. Inaba,[r] T. Inukai,[j] T. Isidori,[l] F. Jonas,[k,s] T. Kawaguchi,[j] R. Keidel,[t] M.H. Kim,[m] V. Kozhuharov,[i] T. Kumaoka,[j] L. Kusch,[a] C. Loizides,[k] Y. Melikyan,[u] Y. Miake,[j] N. Minafra,[l] J. Nystrand,[b] N. Novitzky,[j,k] T. Økland,[b] K. Oyama,[v] H. Park,[j] J. Park,[j] I. Pascal,[e] T. Peitzmann,[h] M. Protsenko,[f] S.S. Räsänen,[o,u] F. Rarbi,[c] M. Rauch,[b] A. Rehman,[b] M. Richter,[b] D. Röhrich,[b] K. Røed,[d] A. Rusu,[k] H. Rytkönen,[o] S. Sakai,[j] K. Sato,[j] A. Schilling,[t] S. Shimizu,[m] M. Shimomura,[n] R. Simeonov,[i] E. Solheim,[d] T. Sugitate,[w] G. Tambave,[x] D. Tapia Takaki,[l] D. Tourres,[c] I. Tymchuk,[f] J. Yi,[p] Z. Yin,[p] K. Ullaland,[b] S. Yang,[b] T. Yokoo,[j] D. Zhou[p] and S. Zillien[t]

[a] *University of Kaiserslautern-Landau (RPTU), Kaiserslautern, Germany*
[b] *University of Bergen, Bergen, Norway*
[c] *Université Grenobles Alpes, CNRS, Grenoble, France*
[d] *University of Oslo, Oslo, Norway*
[e] *University of Copenhagen, Copenhagen, Denmark*
[f] *Bogolyubov Inst. for Theoretical Physics of the Nat. Academy of Sciences of Ukraine (BITP), Kyiv, Ukraine*
[g] *Universidade de São Paulo (USP), São Paulo, Brazil*
[h] *Institute for Gravitational and Subatomic Physics (GRASP), Utrecht University, Netherlands*
[i] *Faculty of Physics, University of Sofia, Sofia, Bulgaria*
[j] *University of Tsukuba, Japan*
[k] *ORNL, Oak Ridge, U.S.A.*
[l] *The University of Kansas, Lawrence, U.S.A.*
[m] *RIKEN, Japan*
[n] *Nara Women's University, Japan*
[o] *University of Jyväskylä, Jyväskylä, Finland*
[p] *Central China Normal University, Wuhan, China*
[q] *Western Norway University of Applied Sciences, Bergen, Norway*
[r] *Tsukuba University of Technology, Japan*
[s] *University of Münster, Münster, Germany*
[t] *Center for Technology and Transfer, (ZTT), University of Applied Sciences Worms, Worms, Germany*

---

[*] Corresponding author.

https://doi.org/10.1088/1748-0221/19/07/P07006

[u]Helsinki Institute of Physics (HIP), Helsinki, Finland
[v]Nagasaki Institute of Applied Science, Japan
[w]Hiroshima University, Japan
[x]Center for Medical and Radiation Physics, NISER, Jatni-752050, Odisha, India

E-mail: tatsuya.chujo@cern.ch

Abstract: We present the performance of a full-length prototype of the ALICE Forward Calorimeter (FoCal). The detector is composed of a silicon-tungsten electromagnetic sampling calorimeter with longitudinal and transverse segmentation (FoCal-E) of about $20X_0$ and a hadronic copper-scintillating-fiber calorimeter (FoCal-H) of about $5\lambda_{\mathrm{int}}$. The data were taken in various test beam campaigns between 2021 and 2023 at the CERN PS and SPS beam lines with hadron beams up to energies of 350 GeV, and electron beams up to 300 GeV. Regarding FoCal-E, we report a comprehensive analysis of its response to minimum ionizing particles across all pad layers, employing various operational modes including different pre-amplifier and bias voltage settings. The longitudinal shower profile of electromagnetic showers is measured with a layer-wise segmentation of $1X_0$. As a projection to the performance of the final detector in electromagnetic showers, we demonstrate linearity in the full energy range, and show that the energy resolution fulfills the requirements for the physics needs. Additionally, the performance to separate two-showers events was studied by quantifying the transverse shower width. Regarding FoCal-H, we report a detailed analysis of the response to hadron beams between 60 and 350 GeV. The results are compared to simulations obtained with a Geant4 model of the test beam setup, which in particular for FoCal-E are in good agreement with the data. The energy resolution of FoCal-E was found to be lower than 3% at energies larger than 100 GeV. The response of FoCal-H to hadron beams was found to be linear, albeit with a significant intercept that is about factor 2 larger than in simulations. Its resolution, which is non-Gaussian and generally larger than in simulations, was quantified using the FWHM, and decreases from about 16% at 100 GeV to about 11% at 350 GeV. The discrepancy to simulations, which is particularly evident at low hadron energies, needs to be further investigated.

Keywords: Calorimeter methods; Calorimeters

ArXiv ePrint: 2311.07413

Contents

1 Introduction **1**

2 Detector prototypes **3**
2.1 FoCal-E: pad layers 3
2.2 FoCal-E: pixel layers 6
2.3 FoCal-H prototype modules 7

3 Simulation setup **11**

4 Test beam setup **13**

5 FoCal-E results **17**
5.1 Pad-layer MIP response 18
5.2 Electron dataset 21
5.3 One-electron event selection with the pixel layers 22
5.4 Pixel-layer hit response to electrons 23
5.5 Pad channel calibration 24
5.6 Electron selection for pad-layer analysis 25
5.7 Longitudinal shower profiles of electrons 27
5.8 Pad-layer linearity and resolution 31
5.9 Pixel transverse shower profiles 36

6 FoCal-H results **39**
6.1 Data processing, pedestal determination and LG-HG matching 40
6.2 Calibration and linearity 40
6.3 Energy resolution 42

7 Summary **44**

A Calibration of the Electromagnetic Forward Calorimeter (FoCal-E) pads **46**

B Inter-calibration of the SiPMs for FoCal-H **49**

1 Introduction

A new instrument in the forward direction, the Forward Calorimeter (FoCal) [1], was proposed for the ALICE [2] experiment at the Large Hadron Collider (LHC). Its main goal is to study the small-x gluon structure of protons and nuclei by measuring direct photons, neutral hadrons, jets and their correlations at very forward rapidity ($3.4 < \eta < 5.5$ with coverage over the full azimuthal angle) in proton-proton and proton-lead collisions at LHC, as well as J/ψ production in ultra-peripheral heavy-ion collisions [3].

FoCal consists of both electromagnetic and hadronic components: the FoCal-E and the Hadronic Forward Calorimeter (FoCal-H), respectively. FoCal-E has two independent subsystems embedded

2024 JINST 19 P07006

in longitudinally segmented modules, where 20 tungsten absorbers, each with about one radiation length ($1\,X_0$), are interleaved with active layers for shower particle measurements leading to a total of about $20\,X_0$. Each module comprises 18 layers of Si pad detectors aimed at providing good energy resolution over a wide dynamic range for measuring the energy of EM showers. Two layers of high granularity Si Monolithic Active Pixel Sensor (MAPS) are added to the stack at the 5th and 10th position to provide the required spatial resolution to identify photons from neutral-pion decays emitted with very small opening angle. The relative position of low and high granularity-layers were determined using simulations and result in good two-photon separation for shower energies from 0.1–1 TeV. FoCal-H consists of a modular transversely segmented spaghetti calorimeter based on commercially available capillary tubes, each containing a scintillating fiber. Groups of fibers are bundled together and read out by Silicon Photomultipliers (SiPMs) making up a tower. The performance of the proposed detector has recently been studied using Monte Carlo (MC) simulations [4].

To achieve the optimal detector design needed for the realization of the FoCal physics program [3], several performance studies of the detector prototypes have been carried out in the past decade. In particular, for the EM component, various prototype detector systems have been designed and tested. These included fully digital calorimeter designs using only pixel sensors [5–7], calorimeter designs using only pad-sensors [8–10] and a combined pixel- and pad-sensor hybrid design [11]. High-granularity calorimeter designs based on silicon sensors with analog readout have previously also been explored and tested by e.g. the CALICE collaboration [12] and by the CMS HGCal collaboration [13]. In fact, the prototype as well as the final FoCal-E, profits from dedicated readout electronics components developed in the context of the above projects. Fiber-scintillating calorimeters based on the capillary tubes have been designed and tested also by the IDEA collaboration [14]. The latter approach simultaneously uses scintillating and clear fibers to be able to measure both scintillation and Cherenkov light, with the goal to better constrain the electromagnetic component of hadronic showers. For FoCal-H, the extra improvement in the energy resolution of hadronic showers that this may bring is not needed, so the present prototype uses only scintillating fibers.

In this publication, we focus on presenting scaled-down prototype systems closely representing individual FoCal sub-detectors, which have been designed, constructed and tested since 2020 to benchmark the simulation studies [4]. Their functionality was first established in laboratory tests and their performance was then measured by collecting data at various particle beam lines. In particular, hadron and electron beams over a large range of energies provided by the Proton Synchrotron (PS) and Super Proton Synchrotron (SPS) at the East and North test beam areas at CERN were used. The tested FoCal prototypes evolved with time closely connected with the development of the final detector design. Details for every prototype system are given in section 2. To model and understand the performance of the FoCal prototypes, a dedicated MC simulation chain was developed, where the realistic material budget of the prototype detectors was implemented. Details are given in section 3, and variations or additional information is provided when the results are discussed. The evolution of the prototype systems through-out the test beam campaigns over the years are described in section 4, with an emphasis on the setup for November, 2022 and May, 2023, which provided the data for most of the presented results. The results related to FoCal-E are presented in section 5 starting with a comprehensive analysis of the response to minimum ionizing particles across all pad layers, employing various operational modes including different pre-amplifier and bias voltage settings (section 5.1). Details about the electron data and event selection of single electrons using the pixel layers are given in section 5.2 and 5.3, respectively. The hit response of the pixel-layers to electrons and refinements to the standard transport model of the detector for the description of the resulting pixel hit distributions are discussed in section 5.4. The pad channel calibration and electron-event selection for the pad-layer analysis are described in section 5.5 and 5.6. The measurement of the longitudinal shower profiles of electrons, mainly using the pad layers, but where possible including pixel-layer information, as well as comparison to simulations is presented in section 5.7. The linearity of the response and the resolution together with respective comparison to simulations is presented in section 5.8. The performance of FoCal-H obtained from hadron beams, where FoCal-E was removed, is presented in section 6, starting with a brief description on the processing of the data, the determination of the pedestal, and the low-and-high gain matching provided by the readout in section 6.1. Linearity of FoCal-H hadrons in data and simulations is discussed in section 6.2, and used to calibrate data and simulations. The corresponding energy resolution in data and simulation, as well as the systematic uncertainties, are presented in section 6.3. A summary of the obtained results is given in section 7. Appendices A and B give details on the calibration of the pad-layer readout and the inter-calibration of the SiPM gains, respectively.

2 Detector prototypes

In the following, detector prototypes developed since 2020 are described. Even though the presented results focus on the later prototypes, we also mention earlier designs. The FoCal-E prototype is instrumented with low and high granularity Si sensors covering an area of 9x8x17cm, which corresponds to one tower out of the 5 towers foreseen in a module of the proposed FoCal-E full setup [1]. For the FoCal-H a small proof-of-principle prototype and then a larger prototype with 9 modules were constructed covering about $10 \times 10 \times 55\,\mathrm{cm}^3$ and $19.5 \times 19.5 \times 110\,\mathrm{cm}^3$, respectively.

2.1 FoCal-E: pad layers

The prototype uses custom-made boards for hosting the individual low-granularity layers (figure 1). Each of the $9 \times 8\,\mathrm{cm}^2$ Si p-type sensors produced by Hamamatsu Photonics K.K. (HPK) in the 6-inch wafer fabrication process, is segmented in a matrix of 72, $1 \times 1\,\mathrm{cm}^2$, 320 µm thick pads. Two additional pads of smaller size are inserted in the array for calibration purposes. The front plane of the sensor is glued to the Printed Circuit Board (PCB) and wire bonded to the read-out electronics via through-holes carrying the lines to the back of the boards. Other cavities are used to connect the guard rings, high voltage, and ground connections. The depletion voltage is achieved by biasing the sensors through the gold-plated common cathode on the wafer back side. More details, as well as the systematic studies of the sensors' electrical properties, can be found in [15].

For the readout, each PCB hosts the HGCROC Application-Specific Integrated Circuit (ASIC) originally developed by the OMEGA group for the CMS High Granularity Calorimeter (HGCal) [16]. The energy deposit in each Si diode is converted into voltage pulses by the low-noise preamplification stage of the chip and later processed by a shape filter. The signal is then fed to the Analog-to-Digital Converter (ADC) of the HGCROC which provides a linear response up to 320 fC, equivalent to about 100 Minimum Ionizing Particles (MIPs). The signal is also discriminated and provided to two Time-to-Digital Converters (TDCs) used to extend the dynamic range via measuring the Time-over-Threshold (ToT) of larger energy deposits. The ToT is measured relatively to a precise Time-of-Arrival

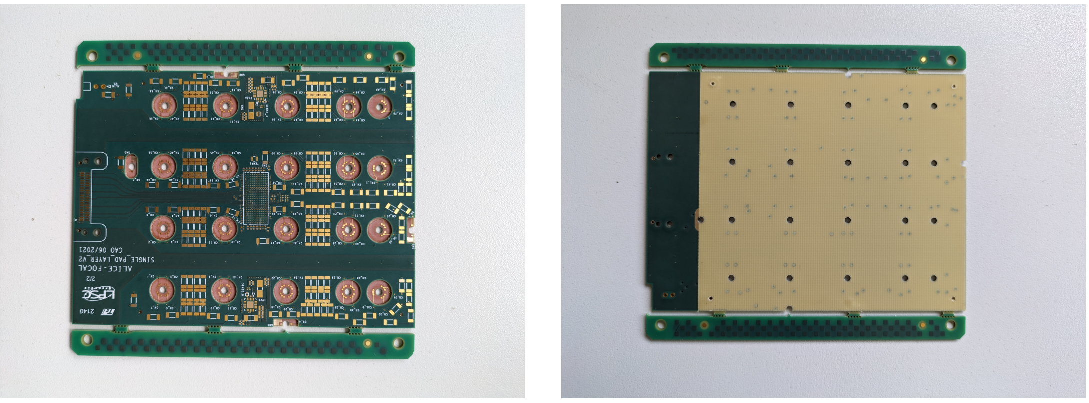

Figure 1. Picture of the front, and back-plane of the single-pad board. The cavities are designed for wire bonding the individual silicon pads to the onboard electronics. At the center, some space is reserved for positioning the High Granularity Circuit ReadOut Chip (HGCROC) readout chip. The Si wafer is aligned and glued to the back-plane, and it receives the voltage for biasing the sensors through a connection routed by the board's edges.

(ToA) information, granting a total dynamic range going from 0.2 fC to 10 pC. These quantities are sampled every 25 ns (40 MHz) and stored in a 512 sample deep circular buffer which is streamed to the acquisition electronics via 1.28 Gbit/s serial links when the HGCROC receives a readout request through the Fast Command (FCMD) port. A buffer entry contains 72+2 measurements of ADC, ToT, and ToA, the monitor of four common mode channels for coherent noise subtraction, and the digital sums of groups of nine pads (eight sums for each sample) for trigger generation. The data streaming operation lasts a total of 1.075 µs since the FCMD signal is received by the chip. To retrieve the correct data from the buffer, the HGCROC has to account for the delay between the readout command and the actual energy deposit in the detector. This can be set through the slow control as a global constant offset in the HGCROC configuration that allows the probing of past recorded entries.

The 18 pad layers sit on an interface card that connects the HGCROCs to the front side of an aggregator board through differential high-speed serial links, and slow control lines shared between groups of five pads. On the aggregator, a XILINX$^{\mathrm{TM}}$ XCKU035-2FFVA1156 Field-Programmable Gate Array (FPGA) is responsible for controlling and monitoring the HGCROC chips of the individual pads, as well as enabling bidirectional communication with the rest of the readout chain through Small Form-factor Pluggable (SFP) modules hosting the optical and Ethernet transceivers. A detailed description of the PCB, the pad-layer design and the aggregator readout card can be found in [17].

The optical transceivers are allocated to interface the GigaBit Transceiver (GBT) links to the ALICE Common Readout Unit (CRU) [18]. Here, the reception link is used to synchronize the detector with the CRU Data Acquisition (DAQ) clock and deliver the Central Trigger Processor (CTP) trigger messages to the FPGA. The Phase Locked Loop (PLL) locks to the recovered clock, and in turn provide the reference for the acquisition firmware. Packets of 80 bits of data containing headers with unique event identifiers are sent to the CRU at every clock cycle (40 MHz) through the GBT transmission link. When a physics trigger is received, the data and the trigger sum information of the 10 previous and 10 following bunch crossings from the HGCROCs are organized in payloads stored in First In First Out (FIFO) memory buffers containing fundamental information, such as the orbit and bunch crossing ID, the trigger type, and possible data drop flag. The output packets are built according to the ALICE Online–Offline Computing System (O2) protocol [19], and transmitted to the CRU.

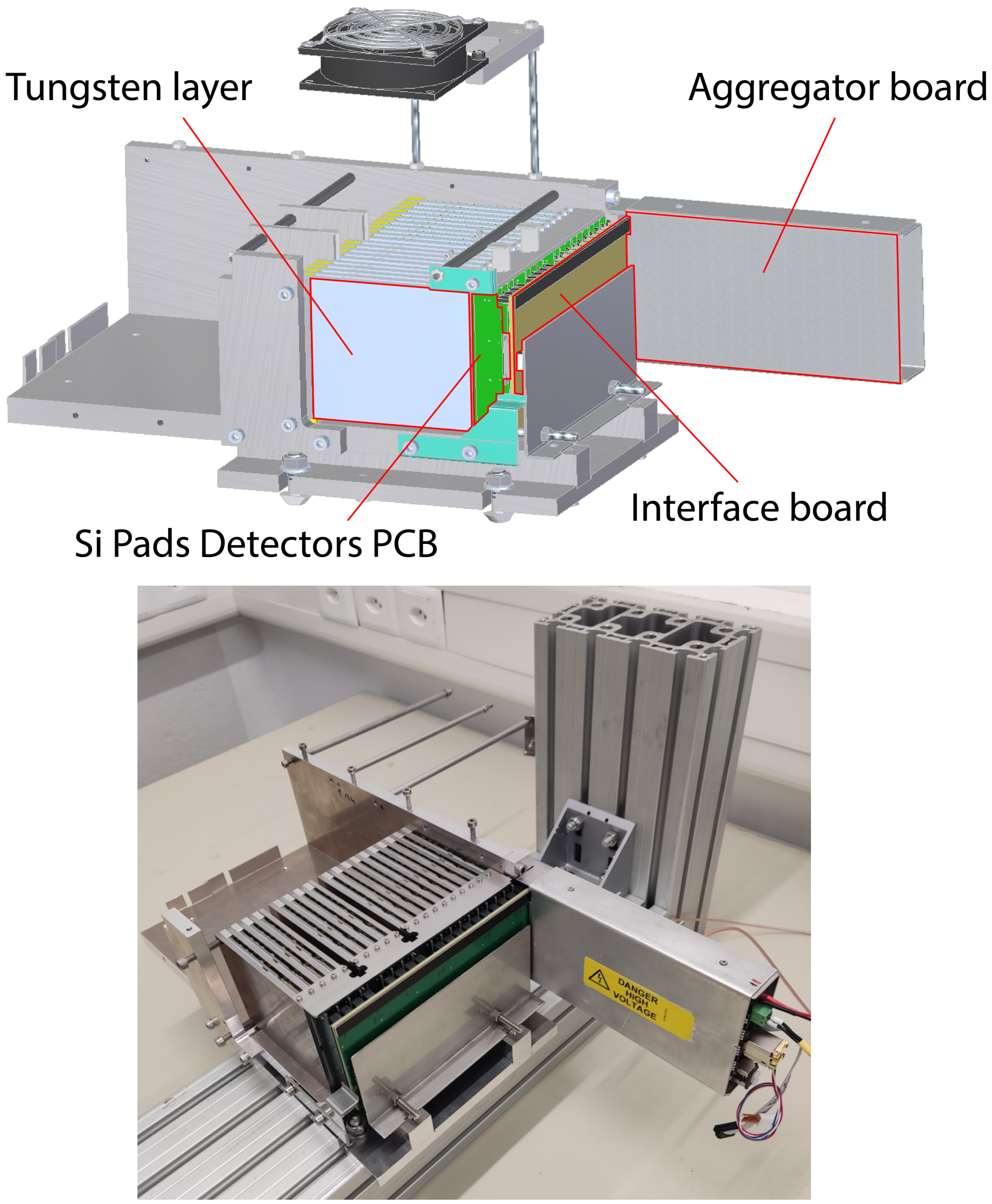

Figure 2. Technical drawing (top) and photo (bottom) of the FoCal-E pad prototype with the interface and aggregator cards on the right. The slots for the pixel layers at position 5 and 10 in the stack are visible and not yet equipped.

An aluminum structure is designed to accommodate the 18 detector layers, as well as the interface and aggregator cards. The tungsten plates are glued to the back of the pad boards creating a rigid structure during the assembly. Empty slots in layer 5 and layer 10 were designed to host the high granularity detectors, described in section 2.2. Two fans are used to mitigate the heat generated by the 20 detector layers and operate the detector at room temperature. This aims to replicate the final detector condition as it will be operated at a temperature of about +20 °C. The full stack is presented in figure 2.

2.2 FoCal-E: pixel layers

The technology of the Si MAPS used in the FoCal high granularity layers is inherited from the ALICE upgraded Inner Tracking System (ITS) [20], which exploits their excellent spatial resolution and low material budget for vertex tracking. The ALICE PIxel DEtector (ALPIDE) is CMOS MAPS produced with the TowerJazz 180 nm imaging process [21]. The sensors have a pitch of about 29 µm × 27 µm, an epitaxial layer for charge collection of 25 µm, and a total thickness that ranges from 50 µm to 100 µm. In the ALPIDE chips, the pixels are arranged in a matrix of 1024 × 512 for a total surface of about 30 mm × 15 mm.

In the ITS, the ALPIDE sensors are hosted on polyimide Flexible Printed Circuit (FPC) referred to as Hybrid Integrated Circuit (HIC). In each module, two HIC half-staves are placed in direct contact with high-thermal conductive carbon fiber sheets embedding polyimide cooling pipes, with rigid mechanical support provided by additional carbon fiber frames. There are two types of pixel sensors depending on their radial distance from the interaction point: Inner Barrel (IB) and Outer Barrel (OB). The two differ in sensor thickness and data transfer rate capabilities provided by the embedded peripheral readout. A detailed description can be found in the ITS Technical Design Report (TDR) [20].

The FoCal design concept uses both ALPIDE readout modes, depending on the radial distance from the beam line, as the expected hit density grows rapidly as a function of increasing pseudorapidity. The central regions of the detector will require the use of IB-mode chips that will benefit from the high-speed dedicated data link operating at a maximum of 1200 Mbps. The peripheral regions will be instrumented with OB-mode chips, where the 400 Mbps data links are sufficient for the lower expected data rates.

As FoCal encounters technical challenges different from the ITS, the proposed mechanical and electrical structure of the pixel layers was entirely redesigned. FoCal inherits its detector blueprint from the digital tracking calorimeter developed for the proton Computed Tomography (pCT) [22], where the ALPIDEs are hosted on single and multilayered flexible microcables based on adhesiveless aluminium-polyimide foiled dielectrics. They are connected to the power, slow control, and data distribution lines using Single point TAB (SpTAB) bonding technology.

Two pixel test prototypes were produced following these assembling techniques. Each layer is composed of two, complementary aluminum carriers hosting three adjacent strings of IB ALPIDE chips (half-layers) glued to the supports. The carriers are then connected back-to-back to enclose and protect the sensors, providing a uniform active area that covers the same transverse acceptance of the pad detectors described in section 2.1. One of the assembled prototypes is shown in the bottom panel of figure 3, while the top panel displays the 3D drawing of the same pixel-layer prototype.

The pixel strings terminate in Zero Insertion Force (ZIF) connectors that route the data, clock, and control lines to the off-detector electronics through an additional PCB. These electronic boards, referred to as Transition Card (TC), communicate with the ITS Readout Units (RU) [20] through a FireFly (FF) differential copper cable assembly solution developed by SAMTEC. The digital and analog power, regulated on the board via a Low-DropOut (LDO), are also routed through the same connectors. The pixel prototypes are finally assembled inside the FoCal-E stack, at nominal position (5th and 10th layer), to provide the tracking information of the Electromagnetic (EM) showers.

To verify the performance of OB pixels at test beam lines, we developed two additional prototype layers based on ITS HICs. In this design, the aluminum carriers envelop three HIC half-layers (a total of six strings) vertically ordered and labeled for simplicity: Top, Middle, and Bottom. In this

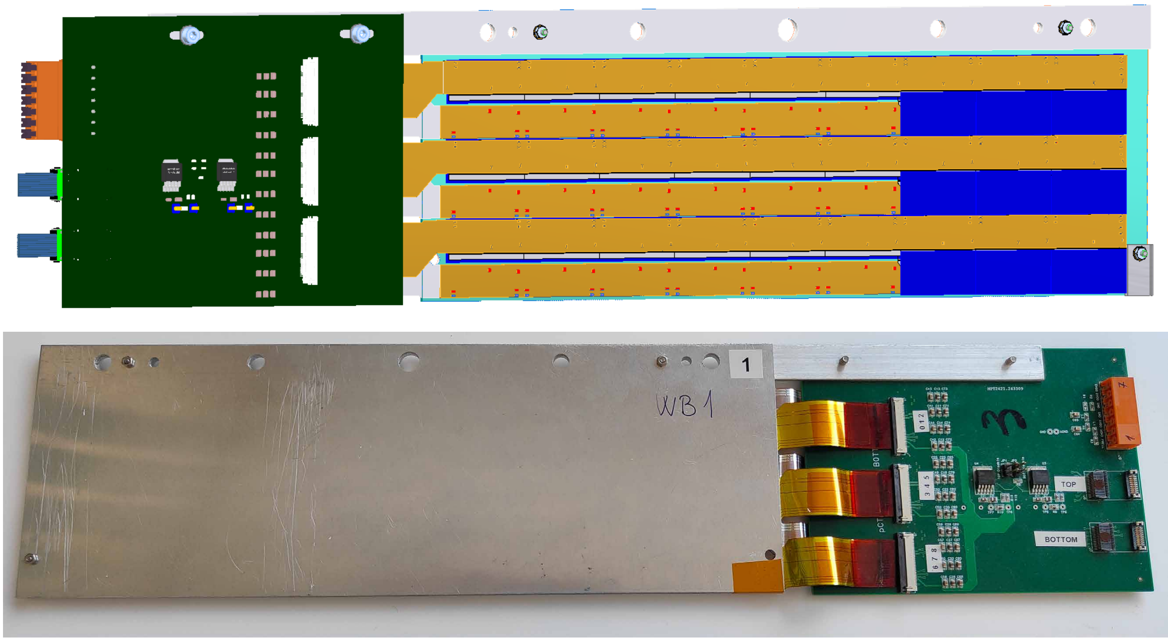

Figure 3. Prototype of the pCT-inspired FoCal-E pixel layer; 3D drawing (top panel) and photo of assembled layer (bottom panel).

version, the pixels closely resemble the ITS stave structure, where the flexible PCBs are directly routed to the readout through a FF. Gold-plated aluminum strips carry the digital and analog power to the pixels, through contacts directly bonded on the HIC PCBs. The HICs are in turn connected to custom-made power boards controlled and monitored by ESP32 micro-controllers used to enable the power delivery and display the current absorption. Figure 4 shows the 3D drawing of an individual HIC layer, as well as the corresponding assembled prototype layer.

2.3 FoCal-H prototype modules

We have built and tested two FoCal-H prototypes each briefly described below. The main focus of the FoCal-H prototypes was to test the conceptual design of the transversely segmented calorimeter based on commercially available copper capillary tubes, scintillating fibers, SiPMs and commercial readout electronics.

The first prototype comprised 1440 copper capillary tubes of inner diameter 1.2 mm and outer diameter 2.5 mm. These were arranged in 40 rows of 36 capillary tubes, with every other row offset by the tube radius to allow the closest possible packing of the capillary tubes. The prototype had a size of $9.5 \times 9.5 \times 55\,\mathrm{cm}^3$, i.e. a height and width of 9.5 cm and a length of 55 cm, half of the nominal length of FoCal-H. The scintillating fibers, BCF10 from Saint-Gobain [23], used in this prototype had an outer diameter of 1 mm and were single cladded. Each of the capillary tubes contained a scintillating fiber, and thirty fibers were bundled together to be read out by a single SiPM. This prototype used ON Semiconductor $6 \times 6\,\mathrm{mm}^2$ MicroFC SiPMs. The reason for the large number of fibers per SiPM was the difficulty in obtaining the SiPMs in 2020 and early 2021: only 48 were available. Two CAEN A1702 [24] readout boards with each 32-channels were used to read the signal of the SiPMs. The prototype was tested on the H6 beam line at the CERN SPS with hadron beams

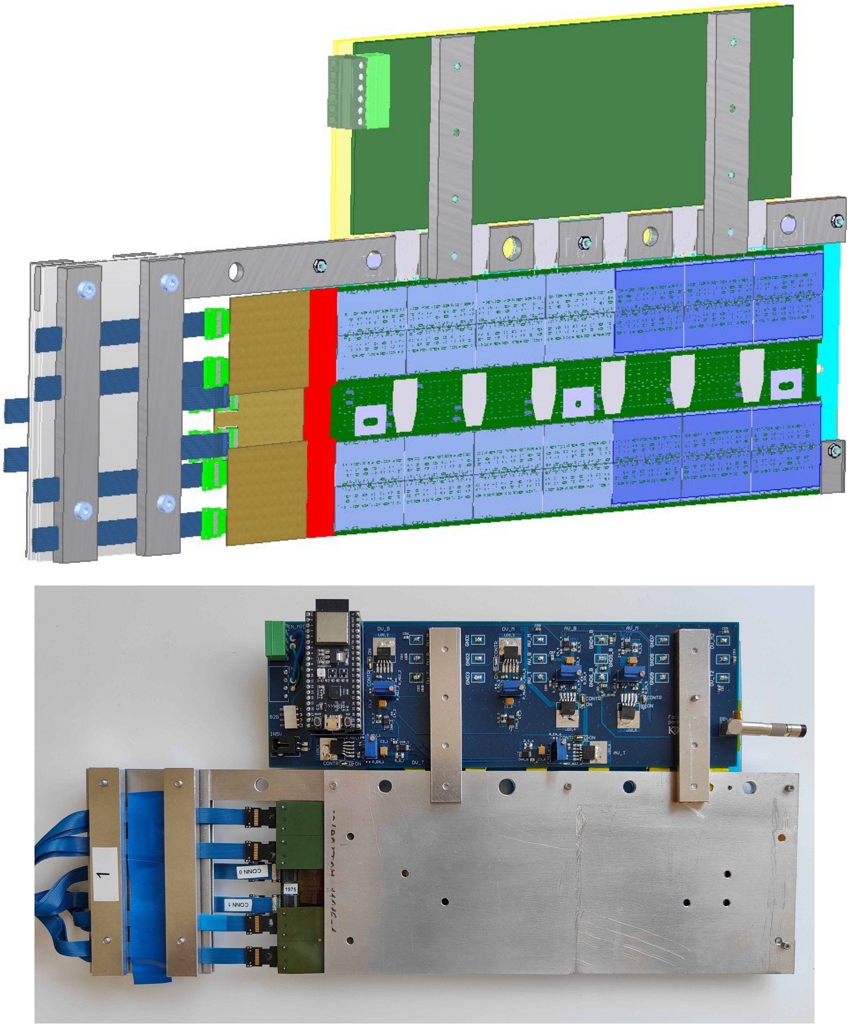

Figure 4. Top: realistic three-dimensional rendering of a single HIC layer prototype. The flexible PCBs hosting the pixels are organized from top to bottom in strings composed by two ITS half-layers. Each one is routed individually to a FF connector. Bottom: picture of one of the two FoCal-E HIC-based pixel prototypes. The three FPCs are connected to the FF cables for the data, trigger, and slow control communication. The monitor and control of the power is enabled through the power board assembled in the aluminum enclosure.

from 20–80 GeV. Further details of this prototype and the results obtained in beam can be found in [25]. The experimental energy distributions were in qualitative agreement with MC simulations, demonstrating the viability of the capillary tube based design.

The second prototype was constructed from 9 modules of size $6.5 \times 6.5 \times 110\,\text{cm}^3$ arranged in a stack of 3 by 3, as shown in figure 5. Each module has 668 copper-tubes with a scintillating fiber inside, with a brass rod in each corner of a module to hold the collector plate for the fibers and SiPM carrier boards. The scintillating fibers in the central calorimeter module were gathered in bundles of $\sim$ 14 fibers read out by 49 SiPMs, whereas the fibers in the outer calorimeter modules were gathered in bundles of $\sim$ 27 fibers read out by 25 SiPMs. The distances between the SiPMs are reduced significantly compared to the first prototype with a separation of 2.5 mm between the edges of the SiPMs used for the outer modules, and 0.5 mm between the SiPM used for the central module. The second prototype, hence, consisted of 249 optically isolated towers, each of which was instrumented with a $6 \times 6\,\text{mm}^2$ Hamamatsu S13360-6025PE SiPM. We used BCF12 [23] 1 mm diameter single cladded scintillating fiber. The performance of this scintillator is similar to BCF10 while the price per meter was slightly lower. Figure 6 shows the assembled prototype calorimeter.

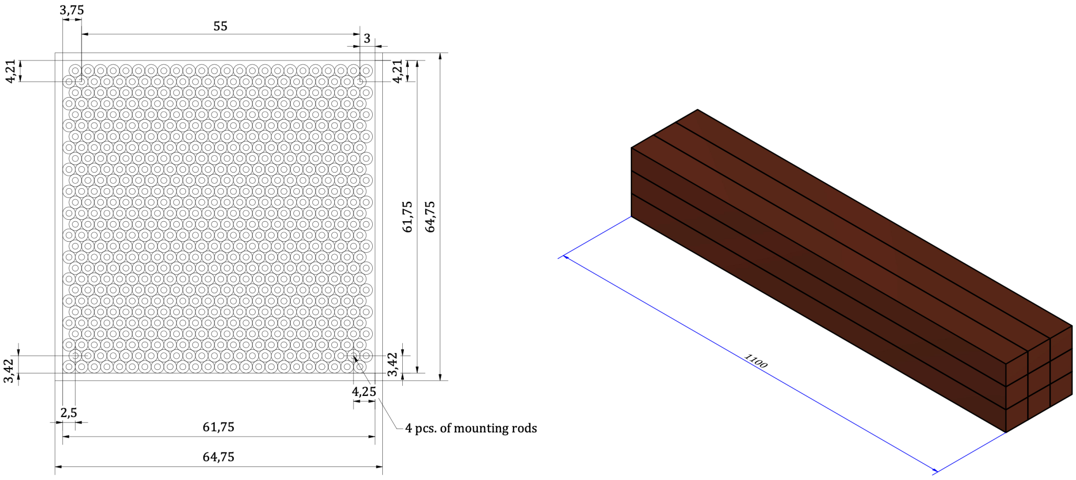

Figure 5. Left: schematic drawing of the design of the calorimeter modules for the FoCal-H second prototype. Right: placement of the 9 square calorimeter modules with respect to each other.

Figure 6. Left and middle: the assembled FoCal-H prototype as a matrix of 3 × 3 modules. Right: the SiPM PCB holders attached to the central module, which comprises 7 × 7 channels, with one PCB removed to show the fiber bundles.

Experience with the first prototype's electronics taught us that saturation of the ADCs would occur in the channels near the center of hadron showers. To mitigate this, a higher granularity for the center module of the second prototype was chosen. Thus, different collector plates were produced for the center and peripheral modules. In the center, the plate collects 49 bundles of 13 or 14 fibers for higher granularity, while in the periphery the fibers are bundled in groups of 26 or 27, and read by 25 SiPMs. The design of the respective collector plate is shown in figures 7 and 8. The SiPMs PCBs were statically screwed to the collector plates. A tight o-ring was placed around fibers and was pushed into the groove in the collector plate to hold the fibers position. The light from the fiber ends traverses a short air gap (below 1 mm) before reaching the SiPMs.

CAEN DT5202 [26] boards designed for SiPM bias and signal processing have been used as the primary data acquition system for the second prototype. Each DT5202 has a pair of Citiroc-1A

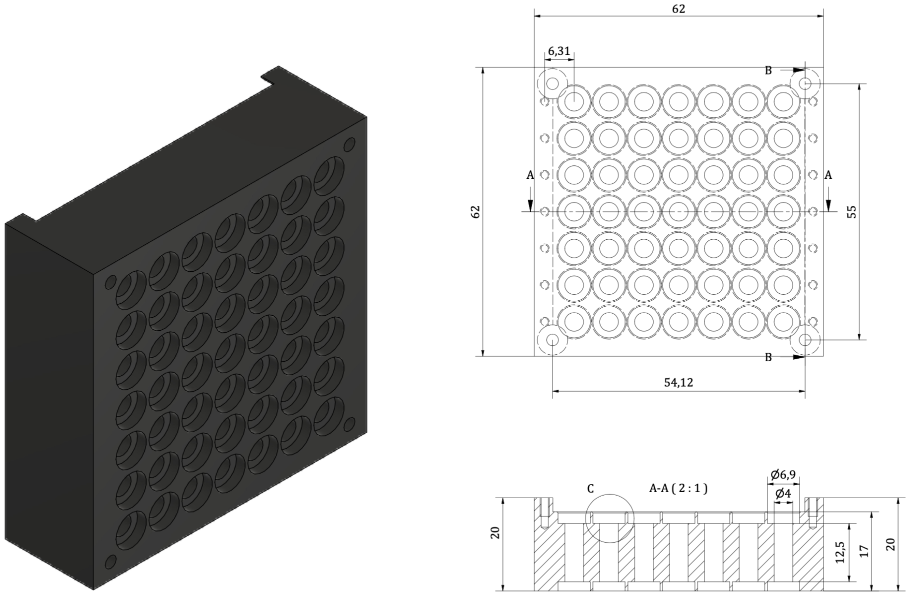

Figure 7. Illustration (left) and drawing (right) of the 7 × 7 SiPM collector plate.

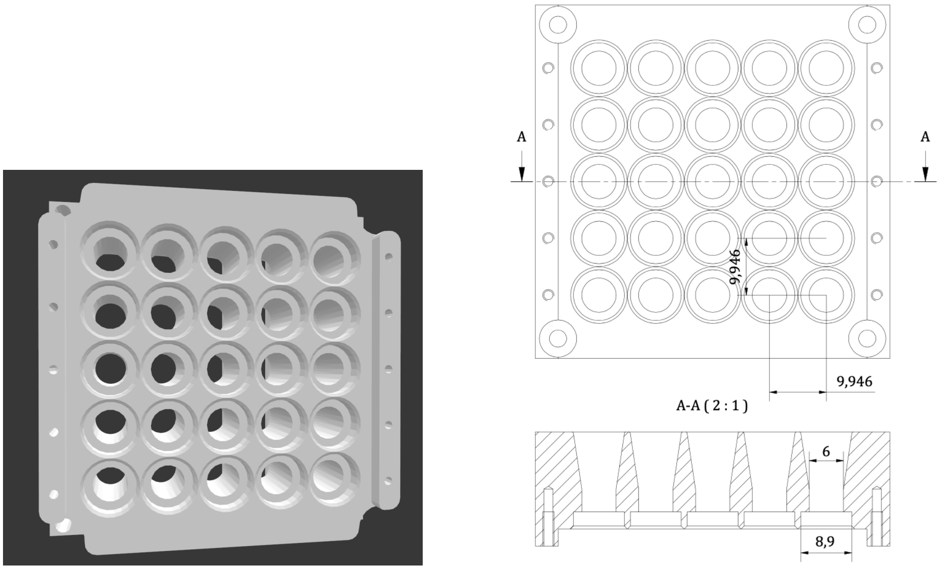

Figure 8. Illustration (left) and drawing (right) of the 5 × 5 SiPM collector plate.

chips [27], for a total of 64 available channels per DT5202 board. The operation of multiple boards was synchronized implementing a common external trigger signal which was processed on-board by selecting one of the available trigger modes. Instrumenting the full prototype requires four CAEN DT5202 boards. Although some early testing was done using fewer boards, these results are not presented here. The communication with the readout electronics was via an Ethernet connection to a dedicated server, which performed the control and monitor of the SiPMs through the vendor supplied JANUS software [28].

2024 JINST 19 P07006

3 Simulation setup

To model and understand the performance of the FoCal prototypes, a dedicated MC simulation was developed using the GEANT4.10.7 software package [29]. The realistic material budget of the prototype detectors was implemented. Figure 9 displays the simulated prototypes.

The FoCal-E simulation setup consists of 20 layers with a 1.2 mm air gap between the layers. Each layer comprises a 3.5 mm thick tungsten alloy absorber and a silicon sensor, where the tungsten alloy consists of 94% W, 4% Ni, and 2% Cu. Out of the 20 silicon sensors, 18 are pad sensors, while layers 5 and 10 are pixel sensors.

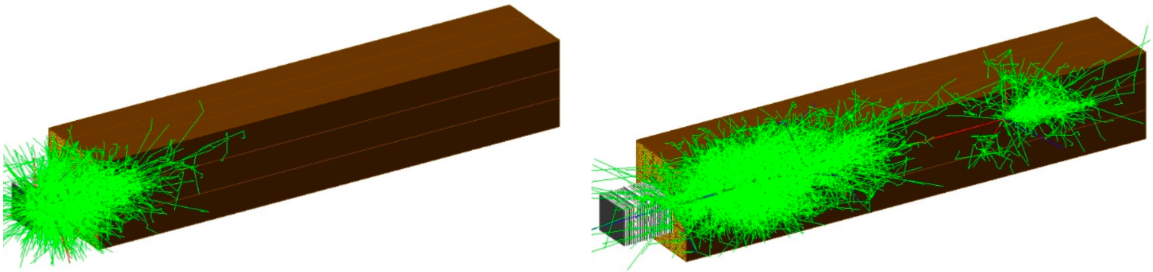

Figure 9. GEANT4 simulation of the FoCal-E and FoCal-H (second version) prototype detectors for a shower created by a 100 GeV electron (left) and pion (right). The incident particle, which enters the detector from the left, is not shown.

The pad sensors have a thickness of 320 μm, with an active thickness of 300 μm. The glue between the tungsten and the sensor and between the sensor and the FPC is simulated as a 1.38 g/cm^3 density epoxy material, with a thickness of 110 μm and 130 μm, respectively. The FPC is approximated by a 140 μm thick uniform Cu layer to account for the electronic components. The corresponding glass-reinforced epoxy laminate (FR4), which has a thickness of 1.595 mm, is simulated as a 1.86 g/cm^3 density material consisting of 47.2% of the same material as used in the epoxy glue and 52.8% of SiO_2. An overview of the materials and their relevant properties can be found in table 1 and table 2. The individual sensors of the pad layers are set as 9 × 8 pads with an individual pad size of 10 × 10 mm^2.

The pixel layers contain two complementary aluminum carriers hosting three adjacent strings containing three pixel sensors each, and three Kapton flex cables interleaved between the pixel strings. In total, they contribute only about 6% of a radiation length. The flex cables are approximated as a 1.42 g/cm^3 density Kapton film, with a thickness of 50 μm. The carriers are connected back-to-back to enclose the sensors and provide a uniform active area. The pixel sensors have a thickness of 25 μm, and the aluminum carriers have a thickness of 1.5 mm. With an air gap of 2.0 mm between the aluminum plates, the total thickness of the pixel layers becomes 5.1 mm. A complete pixel layer contains 18 sensors, with nine per carrier. Each sensor has a matrix of 1024 × 512 pixels with a pixel size of 29.24 × 26.88 μm^2.

The FoCal-H prototype simulation setup consists of nine square calorimeter modules organized in a 3×3 matrix, placed 44 mm behind FoCal-E. Each calorimeter module has outer dimensions of 64.75× 64.75×1100 mm^3 and inner dimensions of 61.75×61.75×1100 mm^3, and contains 24×28 copper capillary tubes filled with polystyrene scintillating fibers. Both the copper tubes and the scintillating fibers are described in detail to account for the shower development and the energy deposition in the different materials of the detector, with only the fibers considered as active volume. The copper tubes have an outer diameter of 2.5 mm and an inner diameter of 1.1 mm. The diameter of the scintillating fibers is 1.0 mm.

Table 1. Overview of the materials used in the pad layers of and their relevant properties (part 1/2).

Stack layer	**Material**	**Density (g/cm^3)**	**Thickness (cm)**	**Weight (g/cm^2)**
Sensor active	Silicon	2.33	0.030	0.070
Sensor inactive	Silicon	2.33	0.002	0.005
Tungsten plate	94% tungsten, 4% nickel, 2% copper	19	0.350	6.650
Glue between W-Si	PET (epoxy)	1.38	0.011	0.015
Glue between Si-FPC	PET (epoxy)	1.38	0.013	0.018
Pad PCB material	FR4	1.85	0.160	0.295
Pad Cu GND layers	Cu	8.96	0.014	0.125
Air	Air	$1.3 \cdot 10^{-4}$	0.270	$3.51 \cdot 10^{-5}$
Sum	**all**	—	**0.850**	**7.178**

Table 2. Overview of the materials used in the pad layers of and their relevant properties (part 2/2).

Stack layer	X **(cm)**	X **(g/cm^2)**	**X/X0 per layer (%)**	E_c **(MeV)**	**R$_\mathrm{M}$ (mm)**
Sensor active	9.37	21.80	0.32	40	4.90
Sensor inactive	9.37	21.80	0.02	40	4.90
Tungsten plate	0.37	6.80	95.44	8	0.93
Glue between W-Si	50.31	44.80	0.02	101	10.50
Glue between Si-FPC	50.31	44.80	0.03	101	10.50
Pad PCB material	16.00	32.20	1.00	63	6.10
Pad Cu GND layers	1.60	12.90	0.88	19	1.60
Air	$3.04 \cdot 10^4$	36.62	0.00	88	7300.0
Sum	—	—	**97.70**	—	—

The *Guide For Physics Lists* by the GEANT4 Collaboration [30] recommends the FTFP_BERT physics list for collider physics application and high energy calorimetry. The guide also mentions QGSP_BERT, the previous default GEANT4 physics list before the default changed to FTFP_BERT in the release of GEANT4 v10.0, as an alternative. Tests were performed using both of the recommended lists. For FoCal-E, there was no difference between the two, while for FoCal-H QGSP_BERT gave slightly more consistent results comparing with the data. Hence, QGSP_BERT was chosen for all of the performance simulations presented in this paper.

For FoCal-H the following corrections are implemented. The energy deposition in the plastic scintillators is corrected according to Birks' law using GEANT4's energy model for electromagnetic saturation. The effect was expected to be small due to the impinging particles' high energy and the relatively small $\mathrm{d}E/\mathrm{d}x$. However, there was a decrease of about 5% in the visible energy with respect to the deposited energy.

A factor of 8000 photons/MeV is implemented to simulate a more realistic light yield for the BCF-12 fibers. Furthermore, to account for the light attenuation, the number of photons from each energy deposit event is corrected with a value of $\exp(-\Delta l/\lambda)$, where Δl is the distance from the position of the energy deposition event to the silicon photomultipliers and $\lambda = 2.7\,\mathrm{m}$ is used, as indicated for BCF-12 fibers. A constant factor of 2.5% is also assumed for the trapping efficiency. This factor considers the solid angle for which total internal reflection occurs and assumes a 100% loss at the non-equipped fiber end. Finally, the light output from each individual hit in a fiber is combined to create a single output quantity from that fiber.

The simulated data is stored in a ROOT format on an event-by-event basis and is further processed by the dedicated analysis and reconstruction module. At this stage, several other effects are considered. The light from individual fibers in the simulation is combined since the fibers in the real prototype are bundled into channels in the readout system. The total light directed towards each of the silicon photomultipliers in the readout is, hence, calculated by adding the light output from each bundled fiber in the channel.

Losses in the number of photons will also occur in the propagation from the fiber ends to the silicon photomultipliers since neither optical silicon nor glue is used between the fiber ends and the front surface of the SiPMs. Here, a factor of 0.5 is implemented to account for the light losses. The photodetection efficiency of the SiPM is assumed to be 0.4. This efficiency is used as a conversion factor translating the number of arriving photons to the mean number of produced photoelectrons. The mean number of photoelectrons is then smeared according to a Poissonian distribution to obtain the number of fired SiPM channels. In addition, the light loss factor and the photodetection efficiency factor were varied between 0.1 and 0.5 each. Due to the high photostatistics at the SiPM, this results has a negligible effect in the energy resolution, which is dominated by the shower fluctuations.

As described, the simulation module assumes a uniform detector response and uniform properties of all the fibers and optical contacts in the constructed prototype. Furthermore, equal gain and photodetection efficiency are used for each silicon photomultiplier. The readout and digitization electronics are also considered to behave linearly and uniformly.

4 Test beam setup

Extensive test beam campaigns have produced the data to compare the prototypes performance with the simulation results and to guide the R&D for the final design. Beams of electrons and hadrons with energies ranging from 1 to 350 GeV provided by various beam lines at the PS and SPS test beam facilities were used to cover most of the possible shower topologies for the electromagnetic and hadronic components of the calorimeter.

Figure 10 summarizes the development of the FoCal prototype systems and instrumentation employed during the test beam campaigns of 2021, 2022 and 2023. Over the years, the tested prototype detectors increased in size and complexity, resembling more and more the prototype of the envisioned final FoCal detector at the end of 2022.

In 2021, two pCT (string)-based pixel layers, and the first prototype of FoCal-H were tested, as well as a single pad layer. The trigger and readout for all systems was independent, making the combination of data between the subsystems impossible.

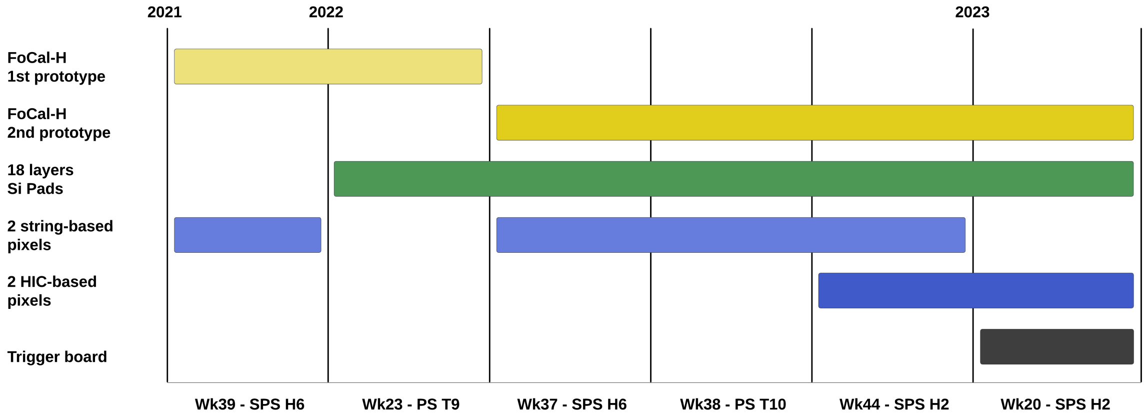

Figure 10. Timeline of the FoCal subsystems and related electronics in 2021, 2022 and 2023. In 2021, additionally a single pad layer was tested to validate the detector performance of the electronics readout.

The situation did not change for the PS campaign of 2022, where the trigger logic of the systems were independent and without possibility of a collective combined data taking. However, for the first time, we operated 18 pad layers in the FoCal-E prototype stack, without the pixel layers. The DAQ of the pad layers was operated in the User Datagram Protocol (UDP) mode, in which commands and data are received and sent through Ethernet connections to a dedicated server. This infrastructure was built to perform the in-beam calibrations and start, stop, and monitor physics acquisitions. A custom-made offline analyzer performed a very preliminary reconstruction of the data to provide a rapid feedback of basic quantities.

In September 2022, the second prototype of FoCal-H as well as the pixel layers were included, as shown in figure 11. The FoCal-E DAQ was based on the ALICE O2 [31] system (explained below), providing coherent treatment of the pixel and pad layers. As described in section 2.3, the readout of the FoCal-H was based on the JANUS software (v2.0.0) provided by CAEN. At that time, rudimentary event matching between the FoCal-E and FoCal-H prototype systems was achieved using timestamps of the recorded events and externally vetoing the data collection while the systems are still busy with the signal acquisition and processing. From the point of the hardware, this completed the FoCal prototype setup.

Refinements and improvements in the DAQ and trigger were done for the data taking periods at the H2 beam line of the SPS in November, 2022 and May, 2023. In May, 2023, an additional custom-made component, the trigger board (described below), was put in place to provide a common acquisition dead time to the FoCal-E and FoCal-H subsystems, and enable a more advanced trigger operation. Figure 12 provides an overview of the May, 2023 setup, displaying the prototype and the associated readout and trigger systems. With the occurrence of a coincidence between the two scintillators placed in front of the setup (displayed in figure 12), the trigger board simultaneously sends out busy signals for the FoCal-H CAEN boards, and provides an external trigger for the Local Trigger Unit (LTU). The LTU emulates the CTP functions of ALICE, providing in turn the trigger at the CRU end-points and enabling the recording of the data for the two systems. The CRUs used to collect the data from the two FoCal-E subsystems are hosted inside the First Level Processor (FLP). These machines are equipped with the O2 software, which handles the detectors readout via the CRU interface and prepares the data for online and offline processing, and ultimately also storage. In the

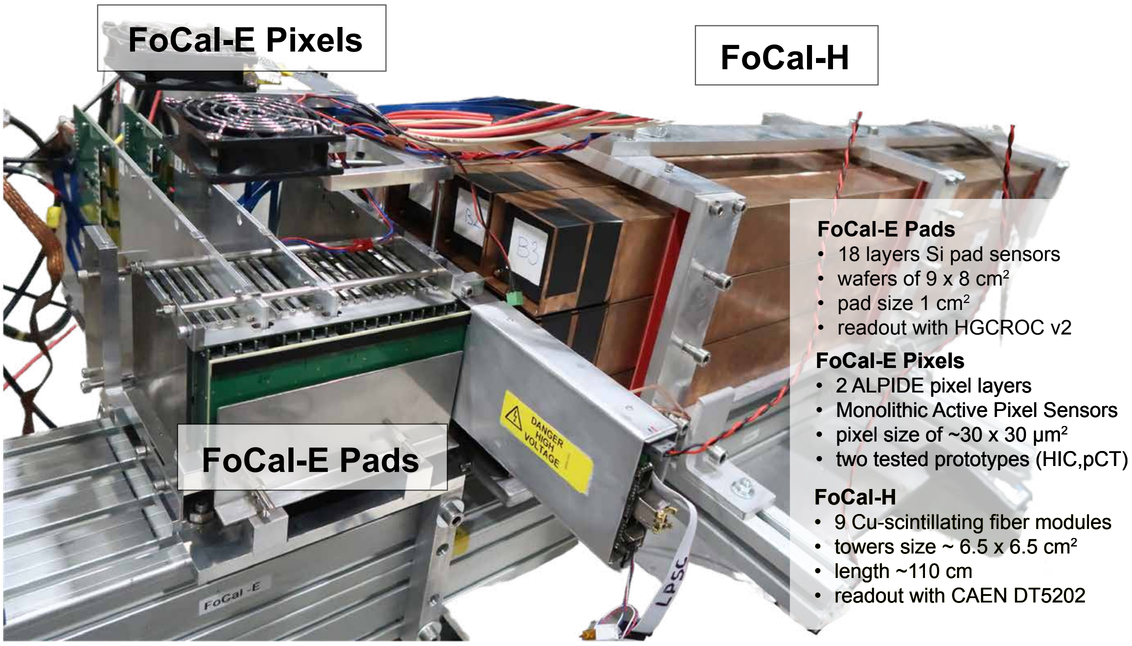

Figure 11. Picture of the full FoCal test beam setup used during the fall 2022 and 2023 campaigns. The FoCal-E consisted out of 18 pad layers, and 2 pixel layers (shown are pCT-based layers but also HIC-based layers were used). The second prototype for FoCal-H was used.

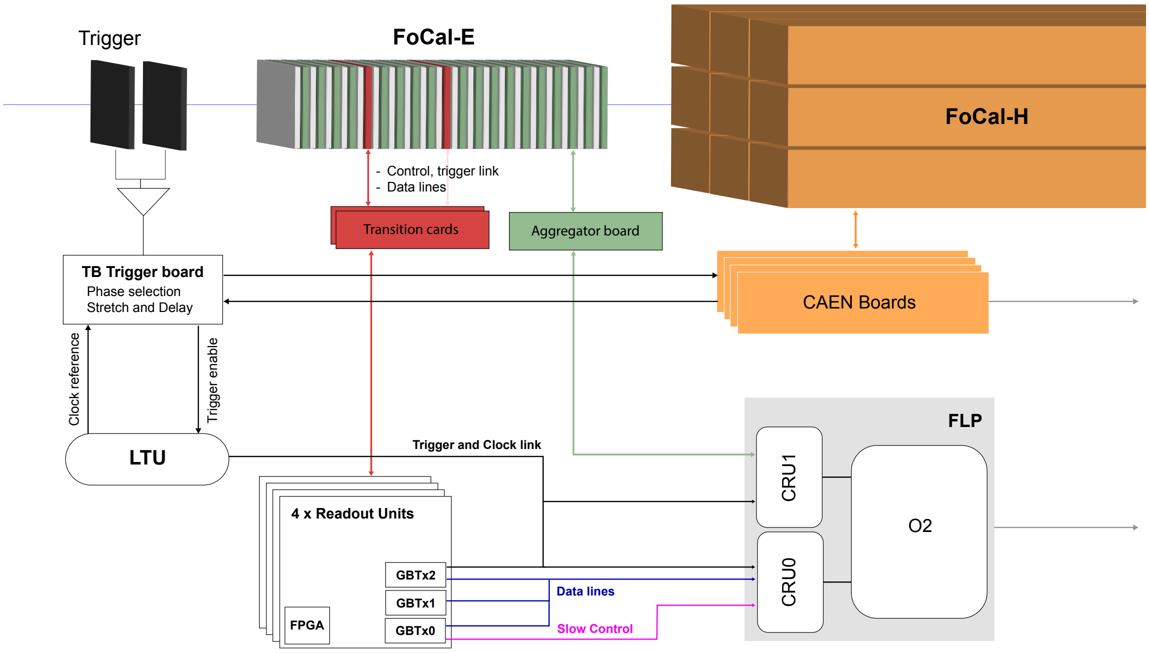

Figure 12. Sketch of the setup at the H2 beam line of the SPS in May 2023. The particles enter the detector from the left to right, having to pass a set of two scintillators used as trigger.

2024 JINST 19 P07006

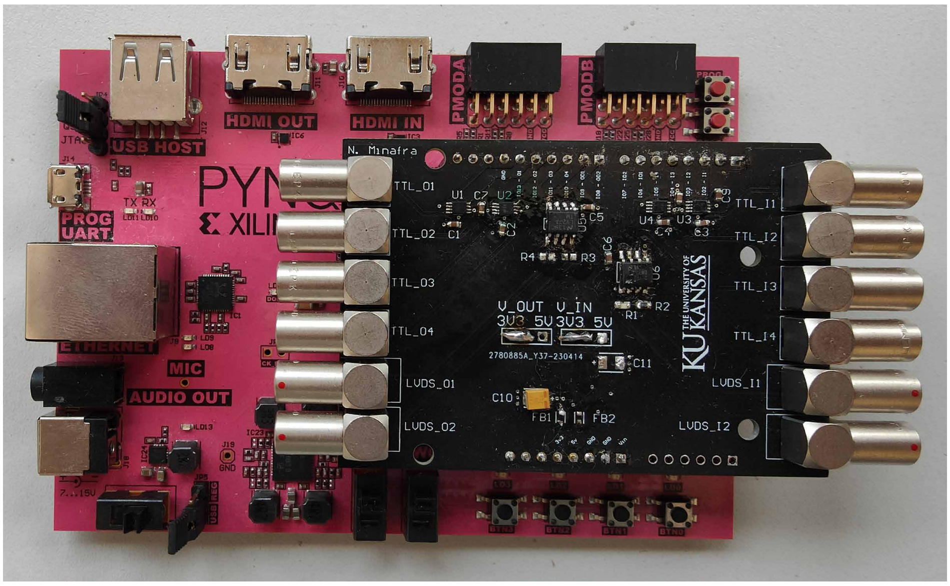

Figure 13. Test beam trigger board assembled on top of the PYNQ Z2 board.

FLP the collected data can be stored locally in the native O2 format, and organized in sequentially recorded time intervals referred to as Time Frames (TFs). At the same time, locally storing the raw data ensures a reliable backup which can prevent data corruption arising from the online reconstruction procedure. The online data-quality monitoring is provided by a detector-specific component based on the Quality Control (QC) workflows which allows to inspect a fraction of the produced data stream. The monitoring objects created by the QC were periodically pushed to a database from which they can be queried and monitored through a web interface.

The trigger board consists of a custom PCB with Commercial Off-The-Shelf (COTS) components that convert the input and output signals to 3.3V Transistor-Transistor Logic (TTL), installed on a PYNQ Z2 board. A picture of the assembled the trigger board can be found in figure 13. The board hosts a Xilinx ZYNQ System-on-Chip (SoC) that uses both a microcontroller and an FPGA. The FPGA was used to implement all the real-time processing, i.e. coincidences, signal synchronization and dead time. The microcontroller was used to implement the control interface using Ethernet and TCP/IP. The board collects signals from 4 different TTL inputs, and can produce up to 4 independent output triggers. Every input can be positive or negative and they can be stretched and delayed digitally to allow an easy synchronization with the other signals. Each signal can also be set as normal input or as a veto. Each output signal can be configured to trigger with a determined pattern of coincidences presented on the inputs. For example, the typical case is with 2 or more scintillators in coincidence and 1 or more busy signals in veto. At the same time, it is possible to limit the trigger rate introducing a dead-time. This feature was particularly useful to guarantee proper synchronization between FoCal-E and FoCal-H during combined acquisitions.

One of the more advanced features is the synchronization of the output triggers with an external clock. For example, it is possible to accept trigger only when in phase with a determined phase of the clock. This feature is particularly useful when testing a system that is designed to work on a beam with bunch structure (like at the LHC), which is tested on a debunched beam (like for most of the test beam facilities). The most obvious application is for the HGCROC ADC, that is sampling at a fixed

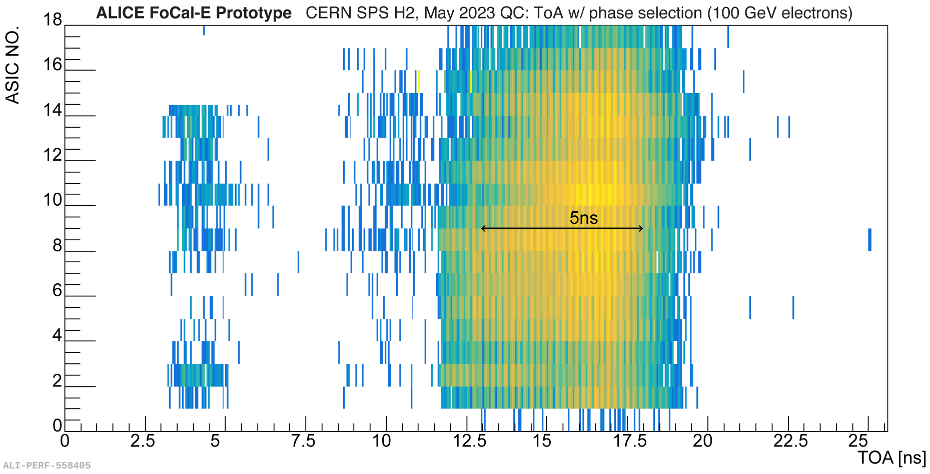

Figure 14. Per-layer ToA distributions for all FoCal-E pad layers after phase alignment measured during a 100 GeV electron run. The plot, extracted online from QC, demonstrates the correct relative time alignment of the 18 HGCROC chips, indicating a healthy working point of the detector.

phase of the 40 MHz clock. When working with a 40 MHz bunch structure, the ADC is sampling always the same part of the signal, ideally the maximum, producing a digitized value that is correlated with the deposited charge. If the particles are not synchronized with the clock, the ADC would sample at a random point of the signal (within the clock period), producing randomly distributed signals. Without the trigger board one needs to record all events with triggering particles and attempt to filter offline all signals that are out-of-time, hence with an unreliable ADC.

This was the approach of all test beams before May, 2023, but it made it difficult and rather impossible to have all the 18 HGCROCs in sync. Using the trigger board, the phase selection was operated using the online monitoring provided by QC. Events where particles arrive in phase with the HGCROC clocks were selected, providing a definite procedure to correctly tune the latency between the event and the readout trigger. As the timing can be independently set on a layer-by-layer basis, the information provided by the online monitoring allowed the adjustment of the relative phases between all HGCROCs. Figure 14 shows the ToA distributions for all FoCal-E pads layers after the phase alignment. The resulting ToA distributions have a spread that is contained within about 5 ns window, achieving a stable working point for the subsequent data analysis. The 5 ns window is due to the fact that the trigger board is selecting 1/10 phase of the clock with a spread of 2.5 ns and a spread from the time-walk of the ToA for signals with no or low ToT value.

5 FoCal-E results

The data for the FoCal-E prototype systems presented in the following were obtained at the T9 beam line of the PS in June, 2022 and at H2 beam line of the SPS in November, 2022 and May, 2023.

The data recorded with the HGCROCs contain the digitized ADC, ToT, and ToA information for every channel of the 18 low granularity layers. In addition, for a recorded event the data payloads contain the timestamp of the event, as well as the trigger information provided by the HGCROC for 20 time intervals (each 25 ns) around the recorded event for every channel.

5.1 Pad-layer MIP response

Standard signal processing techniques are applied to separate the charge deposited by the shower particles from contributions of the noise. The two main contributions to the noise are addressed as follows: the signal pedestal, which results from the combination of the electronics noise in the amplification circuit and the intrinsic fluctuation of the silicon sensors, is treated for each channel by fitting the average response in the ADC with a Gaussian. The width of the Gaussian gives the spread of the noise around the average noise value. The mean of the Gaussian fits are then subtracted to center the reconstructed ADC signal distributions around zero. A second, smaller contribution to the noise results from phenomena equally affecting all the channels of a layer, namely the Common Mode Noise (CMN). This is often enhanced by slower acting effects, such as temperature and bias voltage drifts, however a more impacting source can be identified in the high frequency components coming from the surrounding environment and picked up by the silicon sensors. The CMN is measured event-by-event by sorting the pulse heights of the pedestal-subtracted data in increasing order and selecting the median value. This median value is then subtracted from all amplitudes in the given event. For the MIP analysis, the magnitude of the noise-subtracted signals is used to select the seed channel, by determining the pad with the largest energy deposited for each of the pad layers. Around the seed channel, a cluster of $N \times N$ (with $N = 3$) adjacent cells is used to determine the total energy collected by a given layer, expressed in ADC counts.

A detailed characterization of the FoCal-E pad-layer response was done using low energy (5–15 GeV) hadron beams at the PS in June, 2022 [32]. This included a comprehensive study of the HGCROC preamplification settings and their comparison with the nominal value ranges provided by the ASIC developers. In particular, the feedback passive components of the HGCROC preamplification stage can be modified to attempt the optimization of the detectors Signal-to-Noise Ratio (SNR). A number of combination of the parameters were tested to find the optimal working point of the readout ASICs. A selection of the results for 4 settings (out the 24 reasonable combinations of $\mathrm{R_f}$ in range of 25–100 kΩ and $\mathrm{C_f}$, $\mathrm{C_{fcomp}}$ in range of 50–400 fF) are shown in figure 15. The goal was to choose settings which lead to good separation between the MIP signal and noise. As a result of the study, in particular, the settings “100 kΩ, 300 fF and 100 fF” (black line in the figure) and “50 kΩ, 200 fF and 100 fF” (red line in the figure) were used in the following. The resulting shape of the distribution can be described with a Landau distribution that models the energy deposition in the detector material convoluted with a Gaussian distribution describing the detector’s resolution (called langaus distribution in the following). The Most Probable Value (MPV) of the distribution is usually quoted as the MIP peak (or position) and the width of the Gaussian as the MIP width (or resolution). An example of MIP distribution and fit results for a specific chip and seed channel is shown in figure 16. Results for all channels can be found in ref. [32].

The most probable value and the width of the MIP distributions were studied as a function of the bias applied to the sensors [32]. As can be seen in figure 17, the MIP position (given in ADC) increases with increasing bias voltage, reaching a plateau for bias larger than about 300 V. For all of the reported results in the following, the FoCal-E pad sensors were depleted with an applied bias of 350 V.

Systematically measuring the MIP response provides a reliable feedback for monitoring the stability of the FoCal-E prototype detector under varying conditions. In particular, the MIP studies were repeated with data collected at the SPS beam lines in November, 2022 and May, 2023 to investigate the detector behavior at higher energies. Initially, the pedestal and CMN removal procedures described

2024 JINST 19 P07006

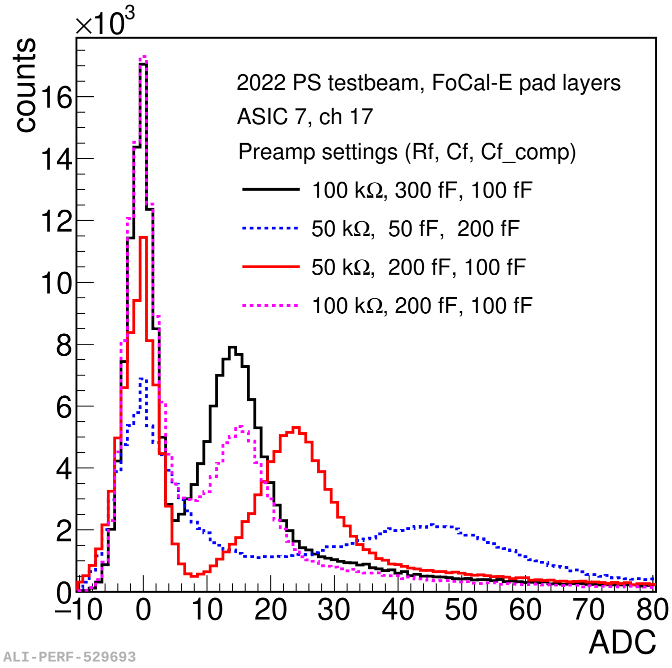

Figure 15. Response from the FoCal-E pads HGCROC gain scan performed during the June, 2022 PS test beam. Shown are 4 out of the 24 combinations of the preamplifier parameter settings. The modified parameters include the feedback resistors and two parallel feedback capacitors.

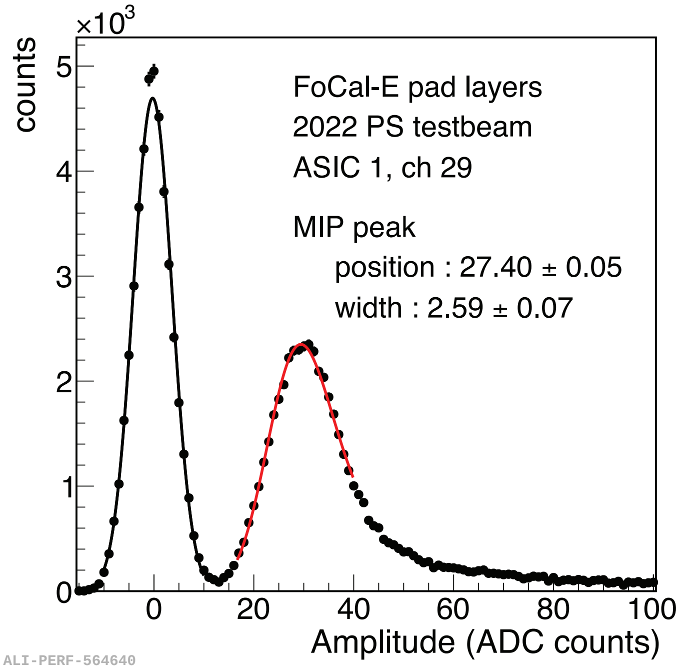

Figure 16. MIP signal in the seed channel (29) the second pad layer (ASIC 1) collected during June, 2022 PS test beam. The data are fit with a Gaussian (black line) to describe the pedestal, and with a langaus distribution (red line) to describe the MIP signal.

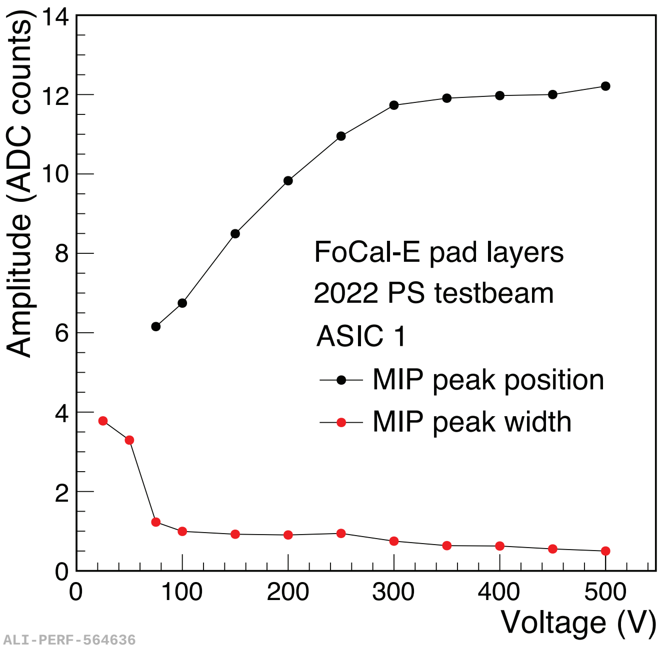

Figure 17. MIP position and width as a function of the bias voltage applied to the silicon sensors for a specific seed channel on the second pad layer (ASIC 1). The data points were extracted from langaus fits of the individual ADC distributions obtained at the June, 2022 PS test beam.

above were performed. Typically, the width of the CMN distribution was about 4.5 ADC counts, and the width of the pedestal after CMN subtraction about 1.5 ADC counts. The MIP position varied by less than 3% in runs with a duration of up to 5 h.

The left panel of figure 18 shows the measured ADC distributions of a specific channel for every pad layer (ASIC) obtained for 200 GeV hadrons at the May, 2023 SPS test beam. Contribution of noise (seen around zero ADC value) can also originate from the response to particles which arrived not well-aligned with the HGCROC phase. To suppress contributions of such events the following additional selection was applied. Provided the position of a seed channel, the pedestals of the first and last layer (ASIC 0 and 17) were fitted by Gaussian functions. The ADC values on both layers are then requested to exceed the average pedestal magnitude by 3σ. The effect of this coincidence cut is shown in the right panel of the figure 18, essentially removing the entries around an ADC signal value of 0. This is also illustrated in the left panel of figure 19, which shows the projection of the ADC distribution for ASIC 2. The pedestal around zero is essentially removed by requiring the coincidence cut. The resulting distribution is fit with a langaus distribution, obtaining an excellent description of the data. The right panel of figure 19 shows the MIP position and width from the fit of langaus distribution obtained after the coincidence cut as a function of hadron beam energy for numerous pad layers (ASICs), demonstrating very little variation over the range from 20 to 350 GeV. The MIP positions are distributed around 10 ADC counts with a variation of about 10%, corresponding to 1 ADC count. This can be attributed to marginal differences in the HGCROC phase settings and tolerances of the components in the detectors readout boards. The MIP width, which is about factor 5–6 smaller than the MPV, does exhibit very little variation between the different ASICs. The corresponding SNR, which can be approximated by the MIP position divided by the width of the pedestal, is 7 ± 1.

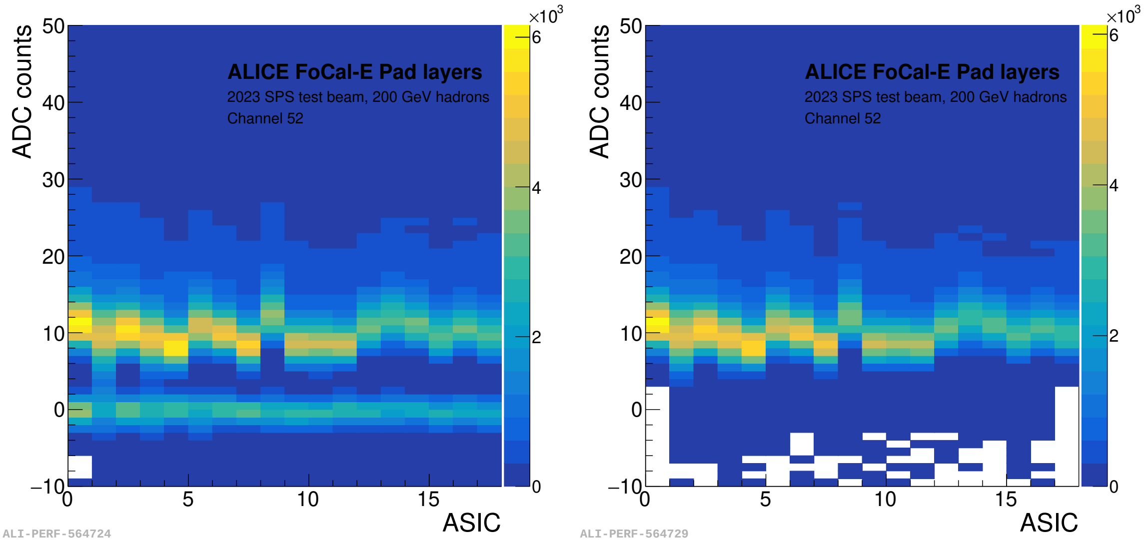

Figure 18. Left panel: ADC distributions of the 18 FoCal-E Pad layers for a given channel (52) for 200 GeV hadrons at the May, 2023 SPS test beam. Right panel: same distributions after requiring the presence of a signal in the first and last layer as explained in the text.

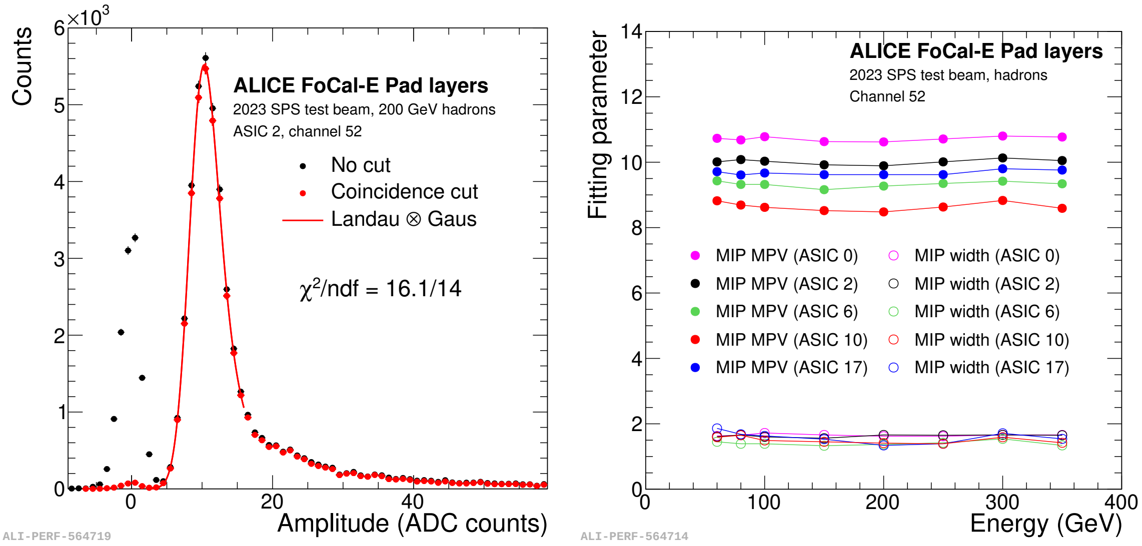

Figure 19. Left panel: ADC distribution for a specific seed channel (52) on the 3rd layer (ASIC 2) for a 200 GeV hadron beam. Black markers are before and red markers (fitted with a langaus distribution) after the coincidence cut (on first and last layer as described in the text). Right panel: MIP position and width for hadrons between 20 and 350 GeV for a specific seed channel (52) for a few pad layers (ASIC 0, ASIC 2 ASIC 6, ASIC10, ASIC 17) after applying the coincidence cut. Data are from the May, 2023 SPS test beam.

5.2 Electron dataset

The electron data presented in the following were recorded in two test beam measurement series at the SPS H2 beam line, in November, 2022 and May, 2023. In November, 2022, electron beams with momenta between 20 GeV and 300 GeV with high purity (electron fraction > 90 % for all energies) were available. In May, 2023, the electron beams were only available up to momenta of 150 GeV, with a significant drop of electron purity at the higher momenta. In November 2022, both the FoCal-E pixel and the FoCal-E pad layers were suffering from few minor technical problems, leading to loss in acceptance. However, the detector was operational, with successful data acquisition. For the pixel layers, the top two horizontal rows of ALPIDE chips did not take data, since no control and data taking could be established to one HIC board via the DAQ system. This lead to an acceptance loss of 2/3 in layer 5, while layer 10 was fully operational. For the pad layers, the ToT channels of one half of layer 7 were found to provide an unstable response during data taking and calibration. It was excluded from all November 2022 analyses, in order to have a clean data sample. The issues were resolved before the May 2023 test beam. For May, 2023, pad layer 7 was replaced with a fully working spare layer, providing a fully functional FoCal-E stack. The full 18 pad layer performance was thus analyzed with the data from May, 2023 up to electron momenta of 150 GeV. In order to study the detector performance over the full energy range, the two data-sets were combined, using energies from 20 to 100 GeV from May, 2023 and energies from 150 to 300 GeV from November, 2022. Here, the layer 7 was excluded in the analyses for both datasets. Since high-energetic electron beams significantly loose energy by deflections in the beam optics, the real beam energies deviate from the nominal beam energies. We used the estimates and uncertainties for the real energies from [33]. In particular, a nominal electron energy of 300 GeV translates to a real energy of 287 GeV, 250 GeV to 243 GeV, 200 GeV to 197 GeV, and 150 GeV to 149 GeV, and the uncertainties on the energies are 0.2–0.3%.

5.3 One-electron event selection with the pixel layers

While for November, 2022 runs, the data were hardly affected by hadronic contamination, an electron candidate selection was necessary for the May 2023 data. Because of the relatively long pulse length of the ALPIDE pixel front-end ($\approx 5\,\mu$s) and the high beam rates, multiple particle events occasionally accumulated in the pixel layers producing pile-up. We therefore select one-electron events with the pixel layers, and use this selection later also for one-electron candidates for the pad-layer data analysis, since the pad front-end has a significantly shorter integration time of about 25 ns. Figure 20 shows the correlation of the number of pixel hits (N_hits) in layer 5 and layer 10 for an 80 GeV run from May, 2023. The two-dimensional representation resolves the various event signatures of one-hadron, one-electron, and multiple-electron events. Since hadrons traverse FoCal-E either as MIPs, which do not shower, or start showering in the first layers, pure hadronic events are characterized by low values of N_hits. In the MIP case only one pixel cluster with an average size of 3 to 4 occurs, and in the hadron shower case the number of hits roughly follows a falling exponential distribution, up to a few hundreds of hits, well below the number of hits in an electromagnetic shower of the same energy, e.g. mostly below 500 hits per layer for a beam energy of 80 GeV as shown in figure 20. At higher values of N_hits, electron shower events appear, well separated from the hadronic events. The regimes of one-electron, two-electron, and three-electron events can be clearly identified. For the data analysis, we require a signature of exactly one electron in the pixel layers. In order to optimize the selection of one-electron events, we employed a two-dimensional cut approach based on the correlation of the number of hits in the two pixel layers. An electron candidate is selected if the number of pixel hits $\{N_{\text{hits},5}, N_{\text{hits},10}\}$ lies inside an ellipse (depicted by the black curve in figure 20), which we define individually for each energy. It thus employs the pixel layers to provide a simple and immediate identification of one-electron event candidates for each beam energy. However, a possible residual contamination by showering hadrons cannot be removed with this method, and remain as a potential background.

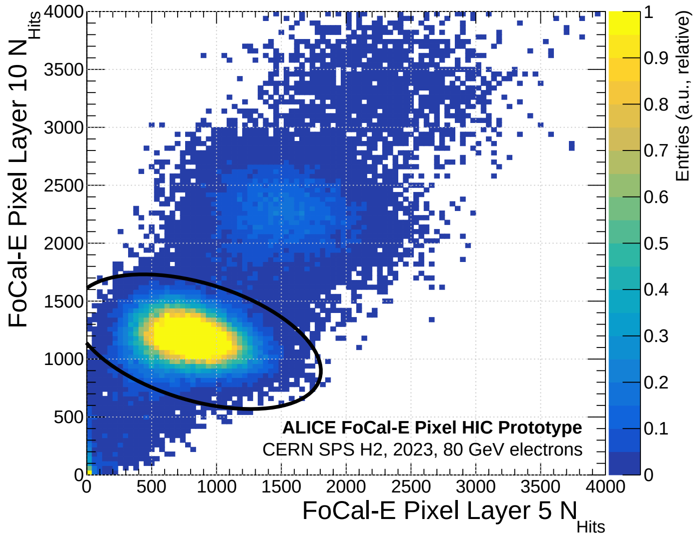

Figure 20. Two-dimensional representation of the number of hits in pixel layer 5 and 10 from the beam test in May, 2023. Single electron events are selected within an ellipse drawn in black.

5.4 Pixel-layer hit response to electrons

Figure 21 shows the number of pixel hits in data and simulations for pixel layers 5 and 10, respectively, at energies of 20 GeV, 100 GeV, and 150 GeV, after the one-electron candidate selection in the data. In the current Geant4 simulation setup, the charge sharing between neighboring pixels is not implemented, and the entire energy deposition process is modeled to occur within a single pixel. The Geant4 simulations will, thus, not generate extended clusters of neighboring pixels since charge diffusion in the epitaxial layer is not simulated. This results in a discrepancy between the simulations (dark blue histogram) and the measured data (black points).

However, creating an accurate description of this process can be extensive and time-consuming. It requires detailed knowledge of the electric field in the epitaxial layer and around the charge collection node, which is non-disclosure material. Instead, a simpler model [34] was implemented as a post-processing step to the Geant4 simulation, in order to reproduce the experimental pixel hit distributions. Additional pixels are generated using an empirical model of charge diffusion in the sensor. The simulated charge deposited in the sensor is translated into the spatial width of the electron diffusion by using an empiric parametrization. This width is then used to derive the pixel cluster size from a two-dimensional Gaussian probability density function.

For each simulated pixel hit, a Gaussian distribution is generated in (x, y) surrounding the hit, where the standard deviation is given as $\sigma_x = \sigma_y = \alpha E_{\text{dep}}^{\beta}$. The Gaussian is randomly sampled N times, resulting in n number of unique pixel hits activated around the originally simulated hit [34, 35]. By varying the parameters and comparing the outcome of the model to experimental data, the following parameters were obtained: $\alpha = 0.17\ \mu\text{m}/(\frac{\text{keV}}{\mu\text{m}})^{\beta}$, $\beta = 0.41$ and $N = E_{\text{dep}} \cdot 11\ \mu\text{m/keV}$, where the energy deposition, E_{dep}, is given in units of keV/μm. The model is applied to the simulated pixel hits with charge information, which are the output of the Geant4 model. The implementation of this post-processing (light blue histogram) step significantly improved the agreement between data and simulation, as demonstrated in figure 21. The data and the resulting MC distributions of N_{hits} were

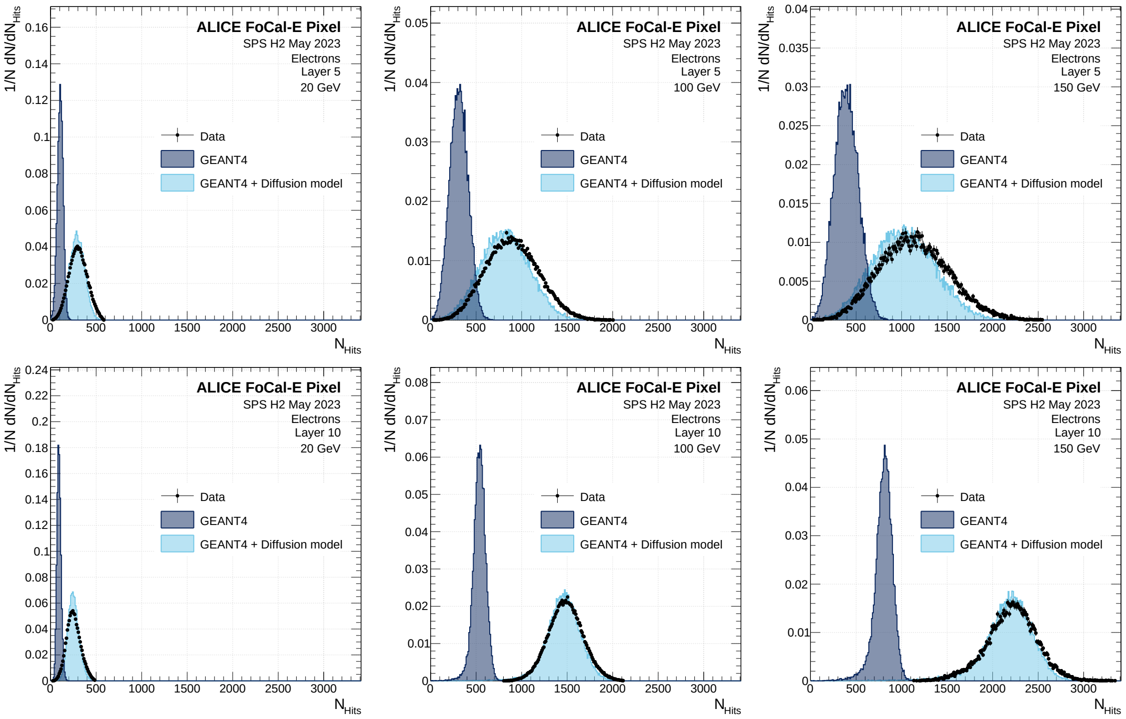

Figure 21. Number of hits distributions for data, GEANT4 simulations and GEANT4 simulations with an applied Gaussian diffusion model as a post-processing step for layer 5 (top panels) and layer 10 (bottom panels) for electron beam of 20, 100 and 150 GeV.

fitted with a Gaussian distribution function, respectively. Per energy and layer, the mean (width) values of the distributions agree on average within 6 ± 5 % (9 ± 10 %).

5.5 Pad channel calibration

Each channel of the HGCROC is equipped with an internal charge injection circuit used for signal response calibration. In order to do so, a known charge amount is injected into the chip through a set of capacitors. One branch of the charge injection circuit uses an 0.5 pF capacitor for *low-range* injection with charges between 0 and 0.5 pC. A second branch uses an 8 pF capacitor for *high-range* injection between 0 and 8 pC. The voltage on the capacitors can be set through an 11-bit DAC-register to a fraction of the chip internal reference voltage, which is 1 V.

We use the low-range charge injection for the calibration of the ADC, and the high-range charge injection for the calibration of the ToT. The calibration measurement is performed by step-wise increment of the voltage at the capacitor, using steps of 5 mV, and releasing 2000 charge injections at each voltage step. The software records the response of ADC, ToT, and ToA per injection.

For low-range injections, the dependence of the ADC on the injection charge is well described by a linear function. We determine the proportionality factor of the ADC with respect to the signal charge from a linear fit whereas the channel-wise pedestal is obtained from dedicated pedestal runs. For high-range injections above ≈ 2 pC, we observe a linear response of the ToT, and use a linear fit function to calibrate the ToT. For lower charge values (in particular in the turn-on region), the response of the ToT does not show the same linear behavior as for the higher charges, and we derive a calibration in this range by linearly interpolating between the ToT response at 0 and 2 pC (where the former one is always zero). The successful channel-by-channel calibrations were then used to convert the response of the HGCROC channels to actual charge deposit in the individual sensor pads.

The ToT and ToA units can be translated directly into the time-over-threshold and time-of-arrival of the charge pulse where 1 ToT unit = 50 ps, and 1 ToA unit = 25 ps. For the chosen preamplifier settings, 1 ADC unit is on average equivalent to 0.28 fC. Further details regarding the calibration procedure can be found in section A.

In the GEANT4 simulation model, the energy deposition per pad (i.e. per channel) is recorded. The energy signal is converted to charge by using the average ionization energy per electron-hole-pair in silicon of 3.65 eV/e-h-pair. A charge collection efficiency of 100 % is assumed, and noise (e.g. from the sensor or the electronics) is not implemented.

5.6 Electron selection for pad-layer analysis

For the electron analysis using the FoCal-E pad layers, both the November, 2022 and the May, 2023 data required a proper event selection. While for November data, events which were recorded with the correct timing with respect to the HGCROC clocks had to be enhanced, the event selection for the May, 2023 data needed to focus on a clean electron sample without hadronic contamination.

In both cases, the datasets were pre-processed based on the HGCROC trigger sum word, which is measured per bunch crossing (i.e. every 25 ns). Each trigger sum word represents the signal sum of nine neighboring pad channels, in a primitive format (with reduced precision [16]). For every recorded event, 8 trigger sums per layer were recorded for offline analysis within 10 bunch-crossing bins around the triggered event. In order to reject out-of-time events, an event is selected only if no charge deposit before the signal bin was detected in any trigger sum word. In particular, this rejected events which were recorded one bunch crossing too early. The decay of such signal charge pulses would still be detected in the signal bin, and would hence distort the dataset. The black histogram in figure 22 shows the charge sum distribution of 80 GeV electrons, for all events which have passed the trigger sum requirement. The charge sum is obtained by summing up the information around the leading cell, in a 5x5 window over all layers. While — due to the high purity of the electron beams — a specific electron candidate selection was not necessary for the November, 2022 data, hadronic events had to be rejected in the May, 2023 data. Electron candidate events are obtained from the one-electron dataset in the pixel layers, as described in section 5.3. The full red markers in figure 22 show the charge sum distribution after having applied the one-electron selection criteria. About 75 % of the events are selected with this criterion, showing a prominent electron peak around 26 pC. The selected one-electron events still show a peak from minimum ionizing particles slightly above zero. We attribute this to events where a hadron triggered the readout and is measured in the pads, and an additional pile-up electron was measured in the pixel layers. In order to estimate the hadronic contamination in the beam (but not for further analysis), we requested the signal sums of the central layers (layer 7–11) to exceed 1.5 times the signal sum detected in later layers (17–20). This condition is sensitive to showers which have their maximum in the central layers of the stack, i.e. to electron showers. The hadronic events are depicted with the blue markers in figure 22. Minimum ionizing particles produce the most probable value slightly above zero. A small residual electron peak remains, which most likely is related to electrons which do not start showering in the first few layers of the pad layer stack, and therefore pass the selection criteria explained above. The green open markers in

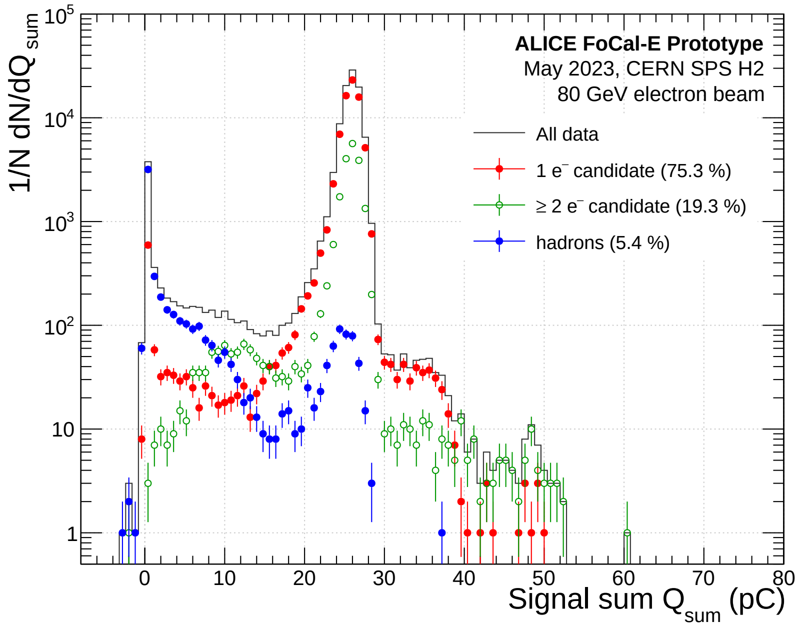

Figure 22. Charge sum (5x5 around leading cell for all layers) of a) single-electron candidates, b) ≥ 2-electron candidates, and c) hadron candidates measured using the pad layers after applying the selection criteria defined by the ellipse cut, and the shower maximum criterion.

figure 22 are the remaining events. They are associated to events where only one electron is recorded in the pad layers, but one or more pile-up electrons are visible in the pixel layers.

Since in the November, 2022 data, triggered events happened asynchronously to the clock of the readout system, an offline phase selection needed to be introduced, making use of the ToA measurements of the HGCROCs. This selection was not necessary in the May, 2023 data, because the phase of accepted triggers was selected with the trigger board (described in section 4). Thus they were aligned synchronously to the readout system clock. The window of the trigger board was measured to have a spread of 2.5 ns, which makes the time-of-arrival of the particle triggers uniformly distributed with a standard deviation of $5\,\text{ns}/\sqrt{12} = 0.72\,\text{ns}$. In the November, 2022 data, instead, events were selected offline only if the ToA in layer 9 was measured to be in a time interval between 1 ns and 1.75 ns with respect to the 40 MHz clock. This selection condition drastically improved the quality of the data, at the cost of a significant reduction of the sample size. Since after the ToA selection, the events are in a certain phase, such that the sampling of the ADC is issued at a constant point in time with respect to the arrival of the particle, the pad-layer response was improved. We have validated the ToA-based phase selection with the 150 GeV electron run from May, 2023. Detailed studies confirmed that at 150 GeV the ToA criterion was not affected by time-walk effects. It can therefore be used as an intrinsic time measurement of the particle's phase of arrival with respect to the clock. We observed that for the lower energies, the shower signal in the leading cell in layer 9 can fluctuate so low that the ToA measurement is not fired (i.e. $\lesssim 0.2\,\text{pC}$). Applying the ToA criterion to these energies would therefore enhance the event selection towards high intensity showers, and introduce a bias to the data. As a result, FoCal-E pad data from November, 2022 at electron energies below 150 GeV are not used for analysis, but replaced with the complementary May, 2023 data, resulting in a combined dataset which covers the full energy range from 20 to 300 GeV.

5.7 Longitudinal shower profiles of electrons

The longitudinal segmentation of the FoCal-E prototype makes the measurement of the longitudinal shower profile of EM showers with a granularity of $\approx 1X_0$ possible. Here, and in the following this is done by measuring the signal charge per pad layer by summing up the information around the leading cell in a 5×5 window (i.e. in a 5 cm × 5 cm square), relating to the charge by using the calibration described in section 5.5.

In the following, we present the longitudinal shower profile measured with the FoCal-E layers for nine different electron energies (20 to 300 GeV). In order to mitigate the effect of transverse shower leakage, only central shower events were used for analysis. The position of the shower center in transverse direction is defined event-by-event from the channel with highest signal in layer 9. Since the beam spot fluctuated on a cm-scale between the various beam energies, three central pads were globally determined which were reasonably close to the beam center for all beams, thus providing sufficient statistics for all analyzed runs. Events are rejected if the shower center is not located in one of the three central channels.

Figure 23 shows the signal sum distributions for each of the 18 pad layers for 100 GeV electron events, compared to GEANT4 simulations (described in section 3). The line shapes of the distributions, which are in general not Gaussian, are in good agreement between the data and simulation. The mean value of the signal-charge per layer is described with the simulation on a ±10 % level for layers 4 to 17.

Example distribution of signal sums for 20–300 GeV electrons versus the shower depth (layer) are shown in figure 24. The longitudinal shower profile is obtained by calculating the average value of the charge sum per layer. It is shown for data and simulations, with the red and black markers, respectively. The longitudinal shower profile can be described by a Γ-distribution [36] plus a small offset correction Q_0 as

$$\frac{\mathrm{d}Q}{\mathrm{d}t} = Q_E\,\beta\,\frac{(\beta t)^{\alpha-1}e^{-\beta t}}{\Gamma(\alpha)} + Q_0. \tag{5.1}$$

In this equation, Q_E is the amplitude which depends on the energy of the primary particles, $t = x/(0.98\,X_0)$ is the depth in the material expressed in units of one layer's radiation length as summarized in tables 1 and 2. The function $\Gamma(\alpha) = \int_0^\infty e^{-z}z^{\alpha-1}\,dz$ is the Γ-function with the parameters α and β which can be interpreted as the shape and scale parameter, respectively. The constant term Q_0 is introduced in order to stabilize the fitting procedure and to account for potential noise contributions in data. The measured and simulated longitudinal shower profiles are found to be well described by the Γ-distribution, as also shown in figure 24.

From the measurement of the longitudinal shower profile in the pad layers, a calibration of the pixel layers can be derived, relating the average number of pixel hits to the measured charge in the pads. The pixel layers are not included for the 60 GeV data because of readout failures for data taken with this specific energy, and neither are they included for the November, 2022 data. For each energy, the fitted Γ-distribution is evaluated at the positions of layer 5 and 10 where the pixel layers are located. The obtained signal charges and their uncertainties derived from the fit function are correlated with the mean number of pixel hits, $N_{\mathrm{hits},5}$ and $N_{\mathrm{hits},10}$. This correlation, shown in the left panel of figure 25, is found to be linear, following the relation

$$Q_{\mathrm{pix}} = (2.39 \pm 0.04)\,\mathrm{fC} \cdot N_{\mathrm{hits}} + (0.02 \pm 0.03)\,\mathrm{fC} \tag{5.2}$$

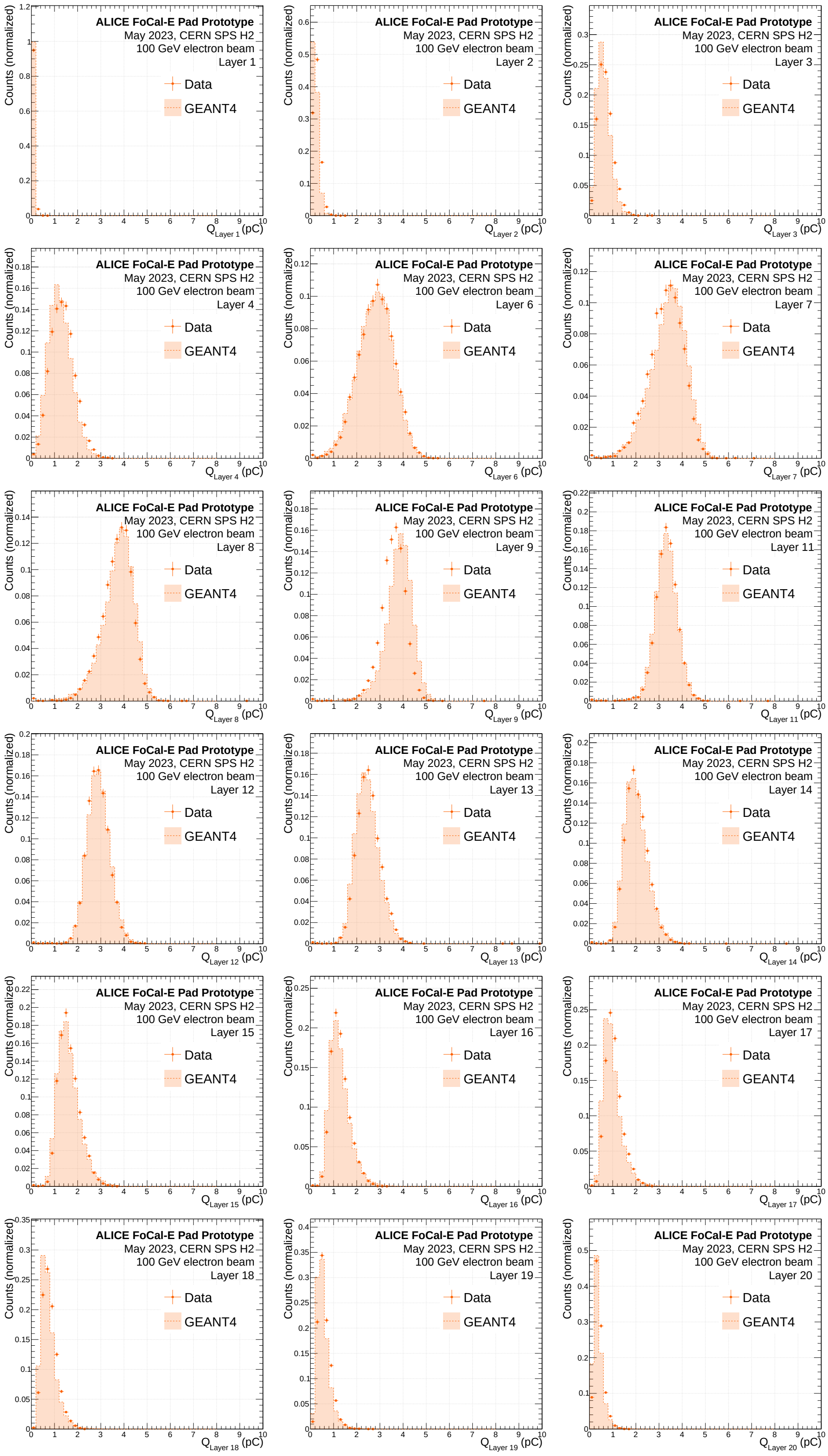

Figure 23. Per-layer charge signal compared to simulation for 100 GeV electrons for the 18 FoCal-E pad layers, recorded at SPS H2 in May 2022.

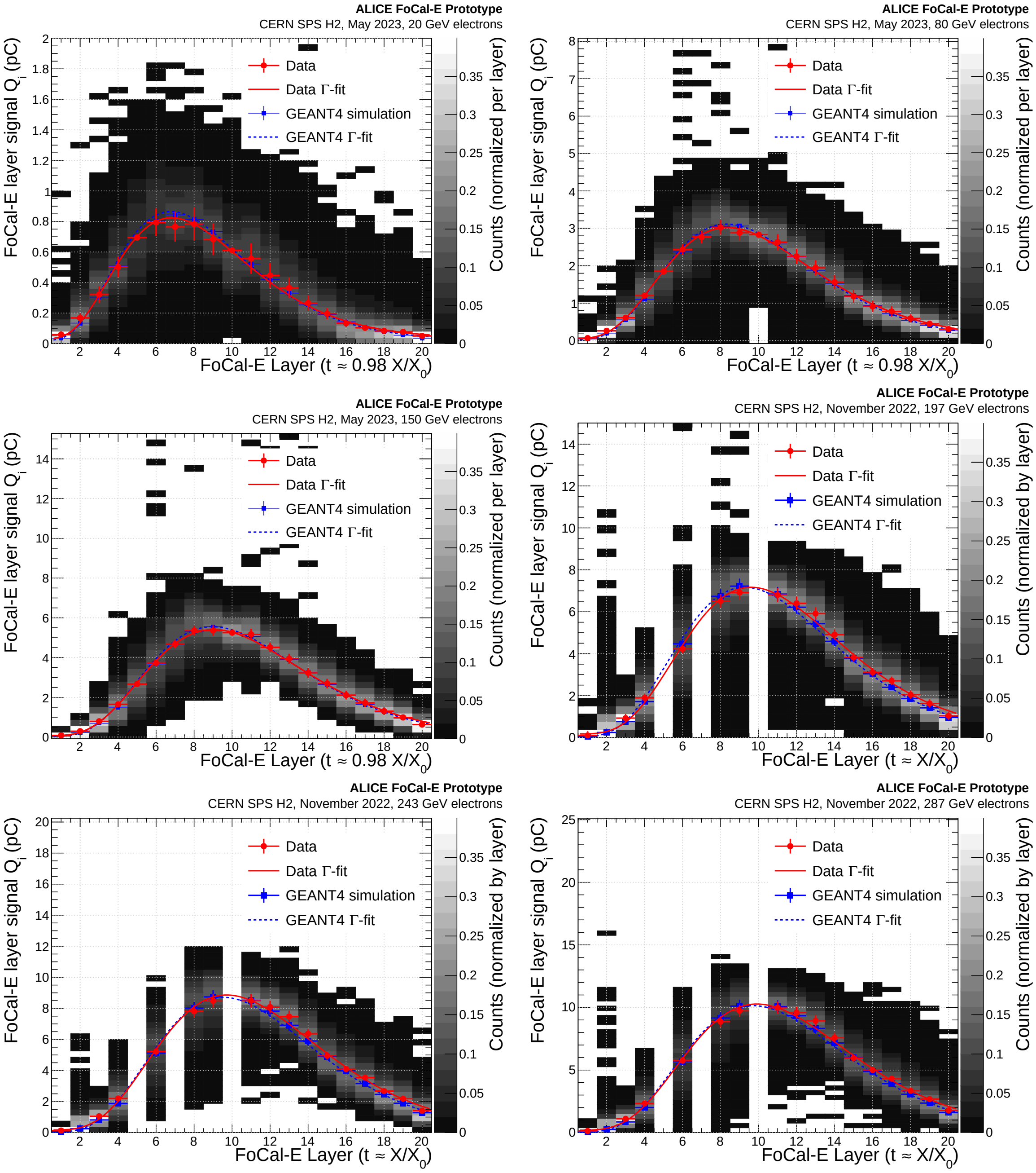

Figure 24. Example longitudinal shower profiles for 20 to 300 GeV electrons. The projections for data and simulations to the vertical axis per layer are identical to the charge distribution measured per layer, as e.g. shown in figure 23 for 100 GeV electrons. Fits to the projections are using eq. (5.1).

with Q_{pix} representing the equivalent pad charge, derived from the signal of the pixel layers. By applying this relation between pixel and pad layers, the pixel signal can be included in the longitudinal shower profile, producing a uniform measurement of the shower profiles with 20 sampling points along the longitudinal shower axis (already done in figure 24). After including the pixel layers, the Γ-distribution fit is repeated, with the fitted parameters listed in table 3. The parameters of the fitted functions are in good agreement with the expectation from simulation, listed in table 4.

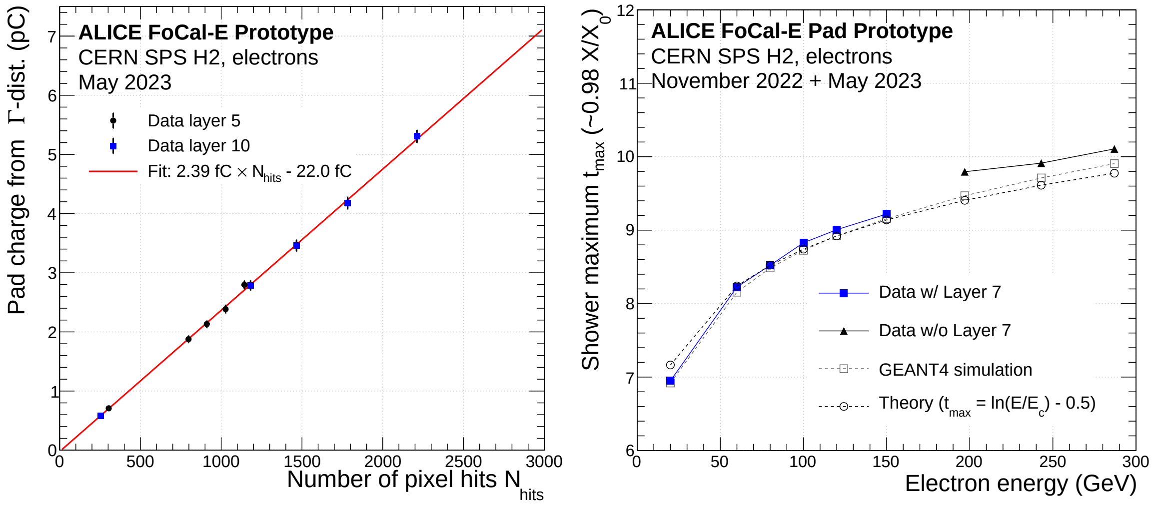

Figure 25. Left: correlation of the FoCal-E pad charge evaluated from the Γ-distribution fit with respect to the number of pixel hits in layer 5 and 10, respectively. Right: the position of the shower maximum compared to GEANT4 simulation and the theoretical value of a homogeneous calorimeter.

Table 3. Parameters Q_0, α, and β for the Γ-distribution fits to data.

E_{nom} (GeV)	$Q_E \pm \sigma_{Q_E}$ (pC)	$\alpha \pm \sigma_\alpha$	$\beta \pm \sigma_\beta$	$Q_0 \pm \sigma_{Q_0}$ (pC)
287	112.85 ± 4.29	6.28 ± 0.32	0.52 ± 0.03	0.20 ± 0.18
243	96.48 ± 4.24	6.17 ± 0.35	0.52 ± 0.03	0.17 ± 0.18
199	74.90 ± 3.95	6.32 ± 0.43	0.54 ± 0.04	0.17 ± 0.18
150	57.73 ± 0.79	5.75 ± 0.11	0.52 ± 0.01	0.08 ± 0.00
120	46.21 ± 0.63	5.56 ± 0.11	0.51 ± 0.01	0.07 ± 0.01
100	38.38 ± 0.57	5.42 ± 0.11	0.50 ± 0.01	0.07 ± 0.01
80	30.80 ± 0.62	5.39 ± 0.15	0.52 ± 0.02	0.06 ± 0.02
60	22.97 ± 0.62	5.23 ± 0.19	0.51 ± 0.02	0.05 ± 0.02
20	7.17 ± 0.26	4.78 ± 0.33	0.55 ± 0.04	0.03 ± 0.01

The maximum depth of the showers is given by:

$$t_{\max} = \frac{\alpha - 1}{\beta} = \ln\left(\frac{E}{E_c}\right) + C_{e,\gamma}\,. \tag{5.3}$$

The left term is obtained after setting the derivative of eq. (5.1) with respect to t to zero and solving for t, while the right term is related to the critical energy, E_c, at which energy losses by ionization start dominating over those by bremsstrahlung [36]. Here, C_i (with $i \in \{e, \gamma\}$) is a constant which depends on the particle species: it amounts to −0.5 for electrons and +0.5 for photons. For E_c we choose a value of 8 MeV, which is the critical energy of pure tungsten. The results on the shower maximum studies are reported in the right panel of figure 25, as a function of the electron energy. The longitudinal position of the shower maximum follows a logarithmic increase with energy, starting from around layer 7 at 20 GeV. It reaches layer 9 at energies above 120 GeV and layer 10 at energies above 250 GeV. This behavior reflects the theory predictions (for homogeneous calorimeters) and is in very

Table 4. Parameters Q_0, α, and β for the Γ-distribution fits to simulation.

E_{nom} (GeV)	$Q_E \pm \sigma_{Q_E}$ (pC)	$\alpha \pm \sigma_\alpha$	$\beta \pm \sigma_\beta$	$Q_0 \pm \sigma_{Q_0}$ (pC)
287	112.33 ± 1.62	6.15 ± 0.08	0.52 ± 0.01	0.04 ± 0.00
243	95.25 ± 1.39	6.08 ± 0.08	0.52 ± 0.01	0.04 ± 0.00
197	77.09 ± 1.12	5.98 ± 0.08	0.53 ± 0.01	0.04 ± 0.00
150	58.52 ± 0.28	5.85 ± 0.03	0.53 ± 0.00	0.04 ± 0.00
120	46.47 ± 1.31	5.76 ± 0.16	0.53 ± 0.02	0.03 ± 0.01
100	38.99 ± 0.18	5.72 ± 0.03	0.54 ± 0.00	0.03 ± 0.00
80	31.05 ± 0.15	5.62 ± 0.04	0.54 ± 0.00	0.03 ± 0.00
60	23.15 ± 0.11	5.48 ± 0.04	0.55 ± 0.00	0.03 ± 0.00
20	7.50 ± 0.04	4.96 ± 0.04	0.57 ± 0.00	0.02 ± 0.00

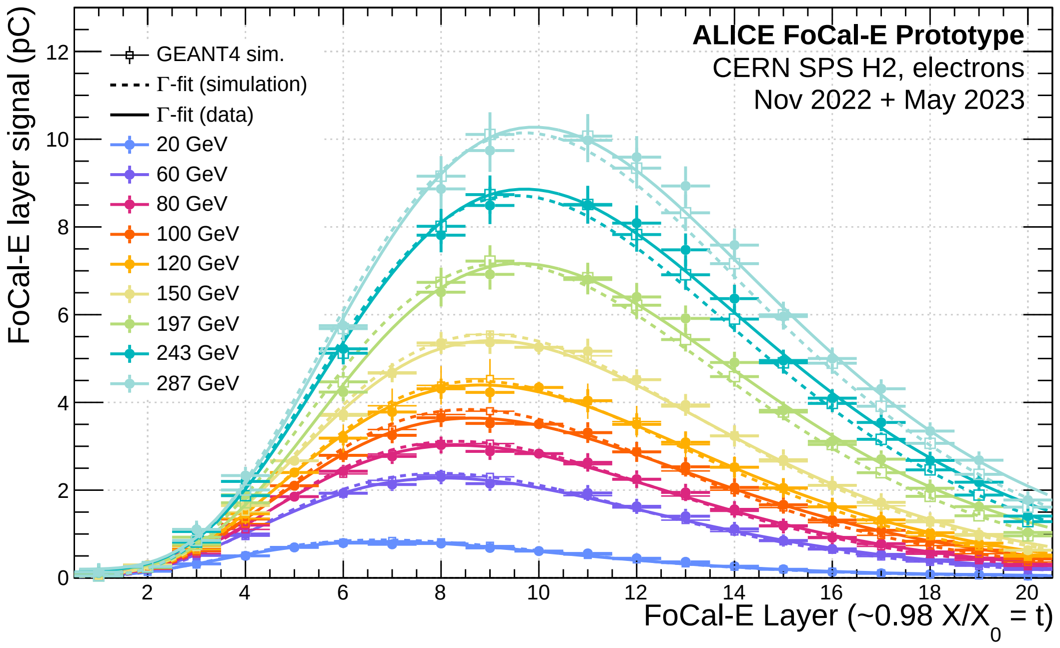

Figure 26. Longitudinal shower profiles for 20–300 GeV electrons compared to Geant4 simulations and fitted with a Γ-distribution.

good agreement with the expectation from MC up to energies of 150 GeV. For energies ≥ 200 GeV (without-Layer-7) the shower maximum is measured slightly deeper in the stack than predicted. The logarithmic dependence on the energy ensures a sufficient longitudinal shower containment in FoCal-E also at higher shower energies.

A comprehensive summary of the measured longitudinal shower profiles is shown in figure 26. The data for electrons of 20–300 GeV are compared to Geant4 simulations, both fitted with a Γ-distribution.

5.8 Pad-layer linearity and resolution

As mentioned in section 5.2, two datasets were defined for the analysis of the detector performance: one covering the full available electron energy range at H2 (20 to 300 GeV) but excluding layer 7 (*without-*

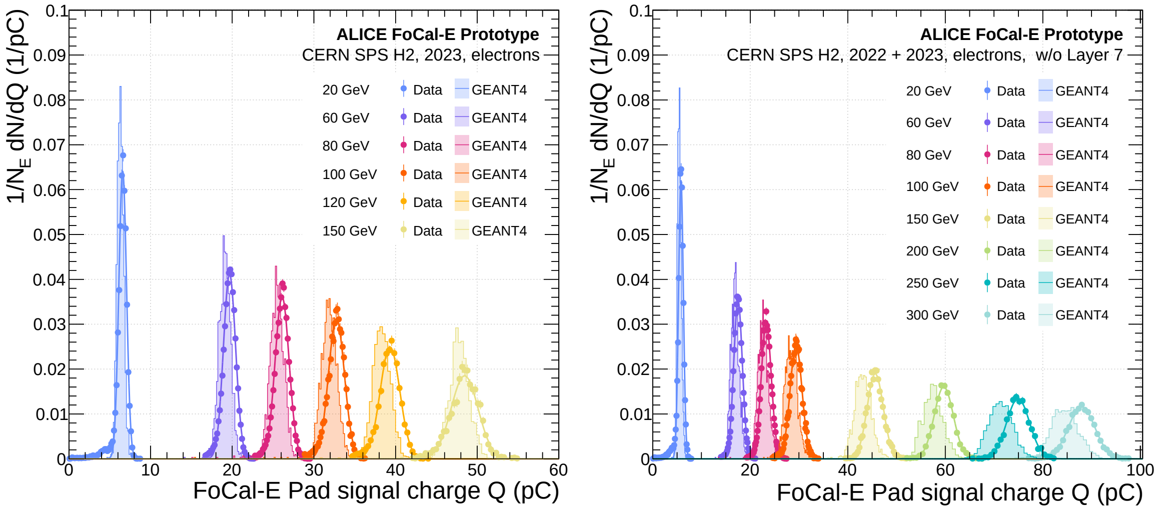

Figure 27. FoCal-E pad signal charge sum distributions for the May, 2023 dataset (left) and the combined dataset from November, 2022 and May, 2023 without-Layer-7 (right). The charge sums are fitted with a Gaussian curve in order to obtain mean and width of the distribution. Outlier points outside the 4-σ region of the Gauss fits amount on average to 1–2 % and are not drawn for better visualization. The GEANT4 simulated samples are drawn with the filled histograms. The bin width of the histograms increases with higher energies.

Layer-7), and one with all layers active (*with-Layer-7*), but only in the energy range from 20 to 150 GeV. In this section we measure the linearity and resolution for both datasets, hence evaluating the FoCal-E performance up to electron energies of 300 GeV.

For the energy response of the pads to electrons the calibrated charge signal in all active pad layers is summed on event-by-event basis, after having applied the electron candidate selection criteria like described above.

The pad signal charge sum distributions for the May, 2023 dataset and the combined dataset from November, 2022 and May, 2023 without-Layer-7 are shown in figure 27. The measured charge distributions are well described by Gaussian curves. For comparison, the distributions obtained from GEANT4 simulations are also shown in each case. The mean, Q, and the width, σ_Q, of the distribution are determined from the fitted Gaussian curves for each energy, both for data and simulation. For the May, 2023 data, the data mean values and the expectation from Monte Carlo agree on the 2 % or better level. For the November, 2022 data, there is a larger deviation ($\approx$ 5 %). Potential sources of the deviations and related uncertainties, e.g. from detector calibration and misalignment of the HGCROC phases could not be fully identified, and the deviation of 5 % was considered as acceptable.

The top panel of figure 28 shows the mean signal charge with respect to the electron energy for data and simulations, and in each case with and without layer 7. Both, data and simulation are well described by a linear fit, $Q(E) = q \times E + Q_0$, as also demonstrated in the lower panel of the figure. The values for the parameters and their uncertainties are given in table 5.

For the May, 2023 data, the slope parameter is fitted to $q = 0.33$ pC/ GeV with the constant offset of $Q_0 = 0.09$ pC compatible with zero, and in agreement with simulations. For the combined dataset without layer 7, the detector response is still linear, despite differences in the response. The parameter q is fitted with 0.307 pC/ GeV, which is 5 % higher than the expectation from GEANT4. The charge offset $Q_0 = -0.52$ pC, however, compatible with the simulation, deviates by $2\,\sigma_{Q_0}$ from

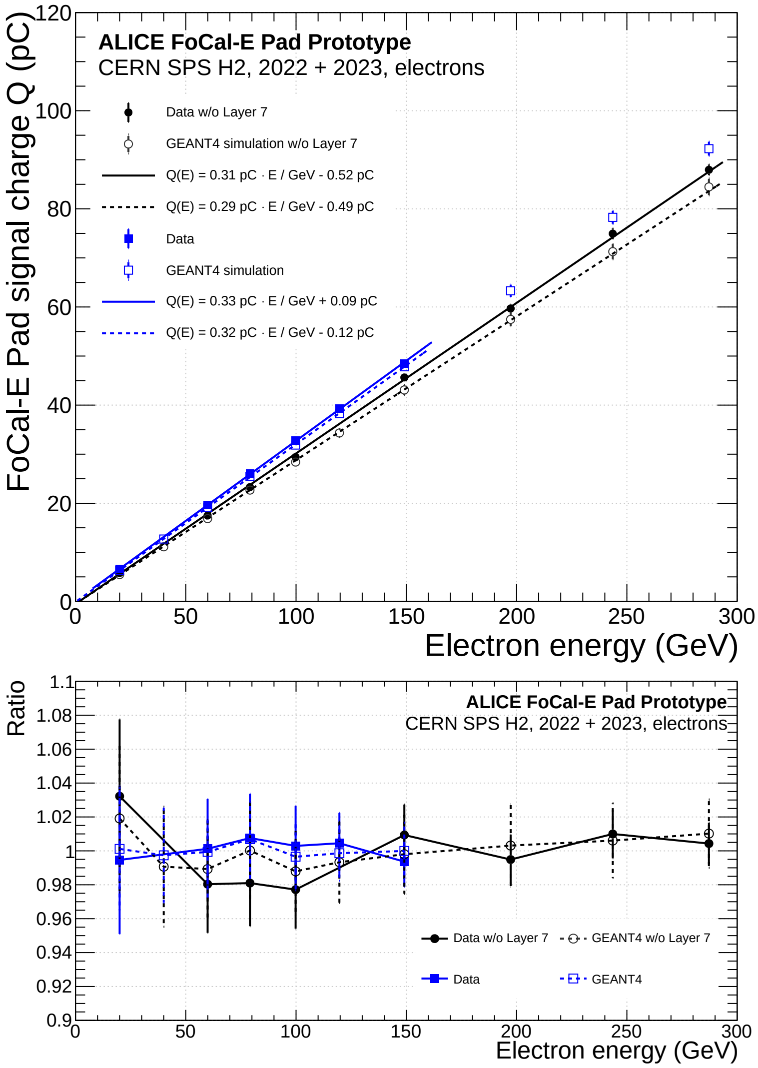

Figure 28. Top: energy response for the FoCal-E pad layers measured with the dataset with-Layer-7 (blue markers) and the combined dataset without-Layer-7 (black markers), compared to simulation (open markers), and respective linear fits. Bottom: ratio of data and simulations to the respective fits.

zero. Since the deviation of Q_0 is also observed in the simulation, it can be attributed to the missing layer 7 information. The missing sampling layer is located in the shower maximum of a 20 GeV shower, but not in the shower maximum of e.g. a 300 GeV shower. Hence, the measured signal is weakened more at lower energies relative to higher energies.

The relative energy resolution of the FoCal-E prototype, r, is defined as

$$r(E) = \frac{\sigma_E}{E} = \frac{\sigma_Q(E)}{Q(E) - Q_0}, \tag{5.4}$$

where Q_0 is obtained from the linear fits just discussed above. The slope parameter q cancels out in the derivation of $r(E)$. Figure 29 shows the relative energy resolution of the FoCal-E pad layers for the two datasets and respective simulations using the mean and σ of the Gaussian fits presented in figure 27. The energy resolution, which is commonly denoted as the result of the quadratic sum

Table 5. Parameters and their uncertainties for the fits of the linearity $Q(E) = q \times E + Q_0$ shown in figure 28.

Dataset	$Q_0 \pm \sigma_{Q_0}$ (pC)	$q \pm \sigma_q$ (pC/GeV)	χ^2	n.d.f.
Data	0.09 ± 0.34	0.326 ± 0.005	0.4	4
GEANT4 simulation	-0.12 ± 0.22	0.322 ± 0.003	0.2	8
Data w/o L7	-0.52 ± 0.26	0.307 ± 0.003	3.5	6
GEANT4 simulation w/o L7	-0.49 ± 0.24	0.293 ± 0.003	1.0	8

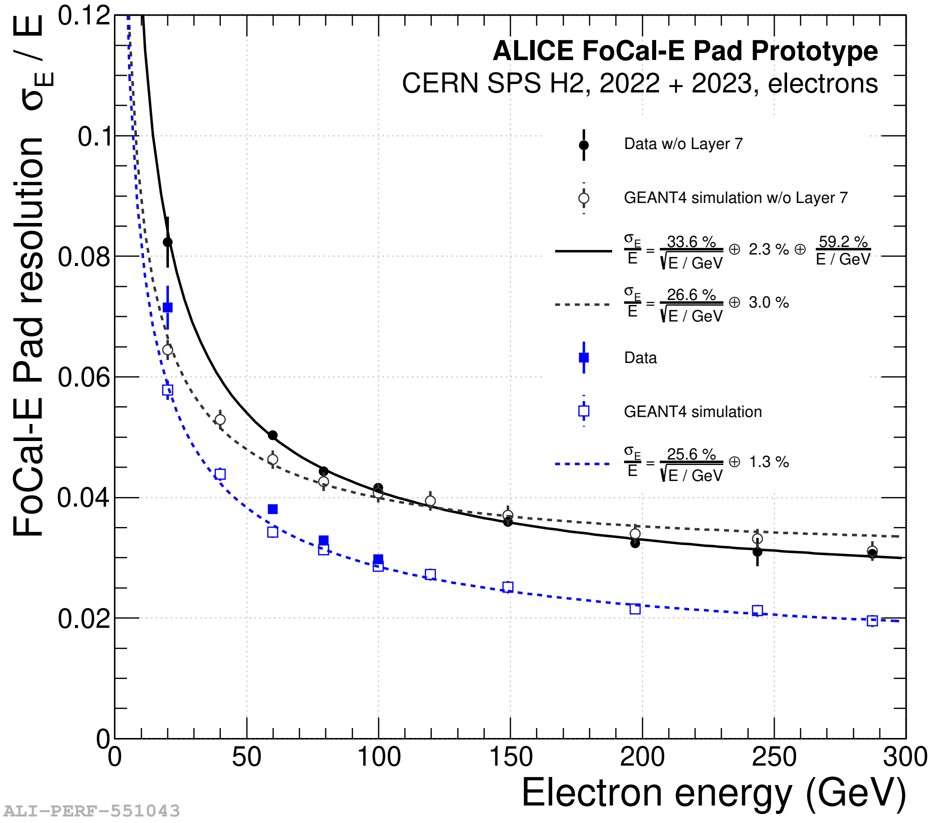

Figure 29. Relative energy resolution for the FoCal-E pad layers measured with the May, 2023 data with-Layer-7 (blue markers) and the combined May, 2023 and November, 2022 data without-Layer-7 (black markers), compared to simulation (open markers), and respective fits.

of three contributions, is expected to follow

$$\frac{\sigma_E}{E} = \frac{\sigma_{\text{stoch.}}}{\sqrt{E/\text{GeV}}} \oplus \sigma_{\text{const.}} \oplus \frac{\sigma_{\text{noise}}}{E/\text{GeV}} \tag{5.5}$$

where σ_E and E are given in GeV and σ_i are without unit. The first term takes into account the stochastic shower fluctuations, the second is a constant term representing general limitations of the detector design and calibration, and the last one describes the contribution of the electronic noise. Numerical results from fits to the combined data, as well as the simulations, shown also in the figure, are listed in table 6.

For the combined May, 2023 and November, 2022 datasets (without-Layer-7), the resolution values for data and simulation start to agree within the uncertainties from energies of 80 GeV and

Table 6. Stochastic, constant, and noise term parameters for the fits of the energy resolution given in eq. (5.5) and shown in figure 29. The abbreviation "w L7" ("w/o L7") refers to data collected with (without) the presence of a working silicon pad sensor at position 7 of the stack. Since noise was not implemented in the simulation, the noise term, σ_{noise}, is not listed for the simulation.

Dataset	$\sigma_{\text{stoch.}}$ (%)	$\sigma_{\text{const.}}$ (%)	σ_{noise} (%)	χ^2	n.d.f.
Data w/o L7	33.6 ± 1.4	2.27 ± 0.10	59.20 ± 35.3	4.4	5
GEANT4 simulation w/o L7	26.6 ± 0.9	2.98 ± 0.13	-	4.6	8
GEANT4 simulation w L7	25.6 ± 0.5	1.27 ± 0.10	-	5.5	8

higher. For energies ≥ 200 GeV we observe the resolution in data and simulations to be nearly constant at ≈ 3 %, with no obvious trend towards lower values, fulfilling already the required performance of 5% [1]. The points at 20 and 60 GeV deviate significantly from the simulated values, i.e. the measured resolution is 1 % higher (in absolute values) than the simulation. One possible explanation is that the charge measurement in this energy regime (especially at 20 GeV) is dominated by pad charges in the order of ≈ 0.5 fC, which lies close to the transition region of the ADC and ToT range. Thus, this charge regime could be affected by additional noise sources, e.g. from the turn-on of the ToT, which are not so dominant in the higher energy regimes. Furthermore, the ToT turn-on region is not well described by the calibration procedure because of the non-linearity there. The fitted curve to the measured resolution data points is given by

$$\frac{\sigma_E}{E} = \frac{33.6\%}{\sqrt{E/\,\text{GeV}}} \oplus 2.3\% \oplus \frac{59.2\%}{E/\,\text{GeV}}\,. \tag{5.6}$$

The fitted parameter for the stochastic (constant) term disagrees with the Monte Carlo by +26 % (+31 %), corresponding to a 4.8 σ (4.4 σ) deviation. However, this mismatch of the fit parameters likely arises from the worse measured resolution at the low-energy data points. In the high energy region, which reflects the constant term better than the low energy region, the performance is found to be as expected from simulation.

For the May 2023 dataset (with-Layer-7), the resolution points are displayed for 20, 60, 80, and 100 GeV with the blue markers using all 18 pad layers. The resolution of the 18 pad-layer stack is measured to be below 3 % at an electron energy of 100 GeV. We excluded the data for 120 and 150 GeV, for which we measured the resolution to be ≈ 3.1 % and ≈ 3.3 %, respectively. This unexpected result was investigated carefully, and could be traced back to additional ToT noise picked up from the switching of the 40 MHz clock in the HGCROC. This might occur if the detector is operated in an unfavorable timing condition. The effect may be enhanced by the presence of the test beam trigger board as we did not observe such an effect in November, 2022. The measured resolution points in the range of 20 to 100 GeV have a similar deviation to simulations as observed for the without-Layer-7 case.

With this knowledge, the performance of the detector can be extrapolated to higher energies. We thus assume that the 18-pad layers prototype may reach an energy resolution performance for electromagnetic showers which follows roughly the fitted resolution curve from simulations at the high tail

$$\frac{\sigma_E}{E} = \frac{25.6\%}{\sqrt{E/\,\text{GeV}}} \oplus 1.3\%\,, \tag{5.7}$$

plus a potential noise term similar to the without-Layer-7 case. We confirmed this projection by scaling the resolution curve fitted to the without-Layer-7-data with the ratio of the with-Layer-7-MC to the without-Layer-7-MC. The resulting curve (not drawn) describes the measured data between 20 and 100 GeV well, and is in good agreement with the with-Layer-7-MC at energies above 100 GeV. We note that for higher electron energies of $\gtrsim$ 500 GeV, longitudinal shower leakage effects will play a larger role. This effect would lead to a reduction of linearity and resolution of the FoCal-E standalone detector as it is, but can be compensated with the measurement of the leaked shower components by FoCal-H.

This study does not incorporate the contribution of the pixel layers to the linearity and resolution of FoCal-E. We have conducted studies on simulation level which indicate that in the lower energy regime ($\approx$ 20 GeV) the signal of pixel layers, in terms of number of pixel hits, contributes linearly to the overall FoCal-E signal, and the energy resolution can potentially be improved in this energy regime. At higher energies ($\gtrsim$ 100 GeV) effects of pixel hit saturation in the shower center play a non-negligible role, and lead to loss of linearity in the FoCal-E signal, thus not improving the resolution.

5.9 Pixel transverse shower profiles

The two pixel layers of FoCal-E at layer 5 and 10 with a pixel pitch of about 30 μm × 30 μm make it possible to resolve the structure of particle showers on the sub-millimeter scale. In particular, this feature will be used to discriminate single photon (electromagnetic) shower events against background two-shower events from π^0 decays [4].

As illustration, figure 30 shows an event display of a 287 GeV electron shower event in pixel layer 5 (left) and 10 (right). The showers are characterized by pronounced cores in the shower center with hit densities higher than 300 (400) pixel hits/mm^2 in layer 5 (10), and are surrounded by tail components with less dense pixel hit occupancy.

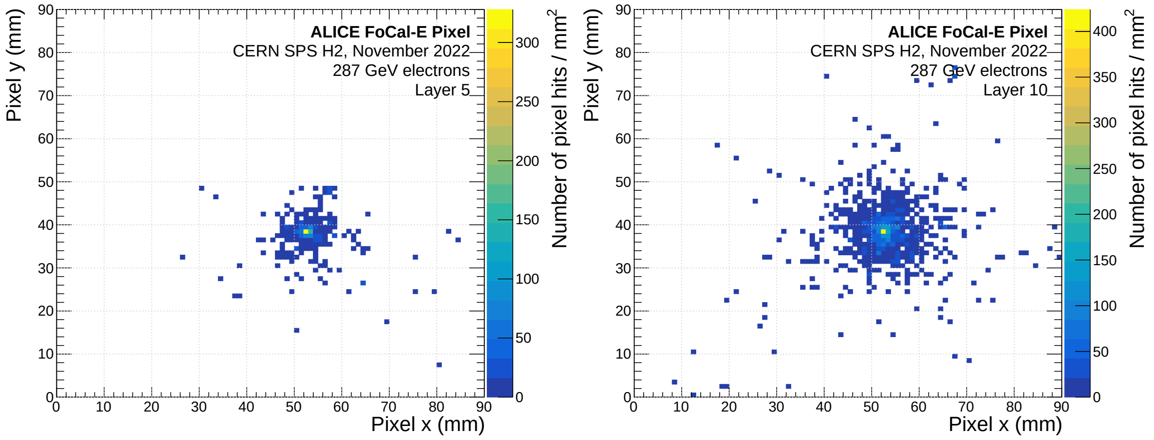

Figure 30. FoCal-E pixel event display of a 287 GeV one-electron shower in layer 5 (left) and layer 10 (right).

As discussed in section 5.3, due to the high electron rate at the SPS H2 beam line and the relatively long integration time of the ALPIDE pixel front-end ($\approx$ 5 μs), we also recorded multiple electron shower events, as shown in figure 31. Two electron-showers are clearly visible, and they can be separated by eye on a scale lower than 1 cm. The event display also illustrates how varying the longitudinal development of a shower in the calorimeter can be: in layer 5 the left shower produces higher occupancy in the core, and in layer 10 the right shower deposits more hits. In the final

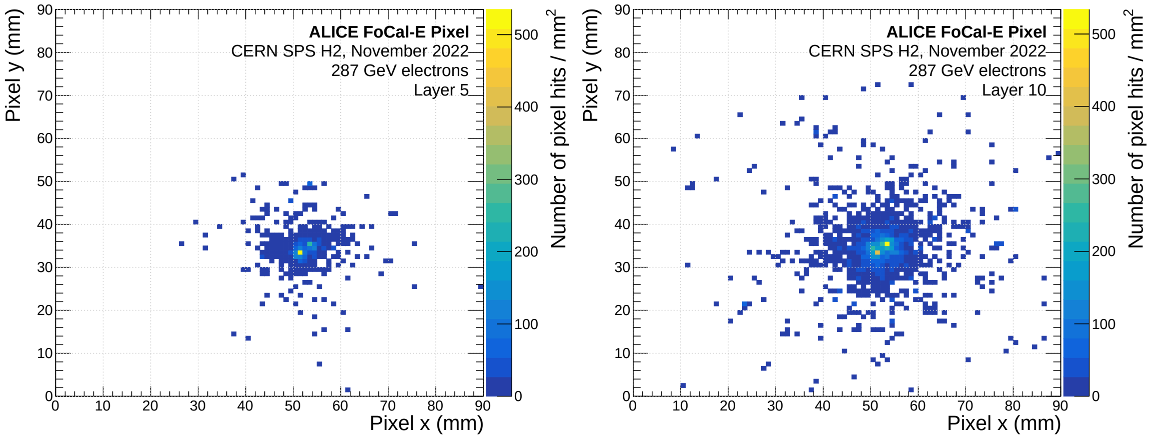

Figure 31. FoCal-Epixel event display of a 287 GeV two-electron shower in layer 5 (left) and layer 10 (right).

detector, rather complex clustering, particle identification and shower separation algorithms will be implemented, to make a decision on a) whether there are two nearby showers in the event, and b) how to share the energy fraction between the two showers. Since for the discrimination of two nearby showers the lateral hit density profiles are one of the key parameters, we present here a study of the transverse electromagnetic shower profile obtained with the pixel layer information.

In order to study the shower profile, we project the hit density distribution to a lateral axis in the pixel layer plane, and measure the functional form $f(\Delta x)$ of the number of pixel hits, N_{hits}, in dependence on the lateral distance Δx from the shower center x_0 as

$$f(\Delta x) = \frac{1}{N_{\text{hits}}} \frac{d}{dx} N_{\text{hits}}(x - x_0)\,, \tag{5.8}$$

where the x-axis is identical to the horizontal direction in the setup. When calculating the distance from a shower-particle hit i from the shower center, $\Delta x_i = x_i - x_0$, the dominating uncertainty originates from the uncertainty on the shower center x_0, i.e. $\sigma_{\Delta x} \approx \sigma_{x_0}$, whereas each single point x_i is measured with high spatial resolution.

To determine an approximate position for the shower center, pixel hits from a single event are filled into a histogram (or “hitmap”), which is binned into macro-pixels of size 40×40 pixels ($\approx 1.1 \times 1.1$ mm^2). We calculate the shower center from the weighted mean position of the macro pixels, where we take only macro-pixels into account which contain a minimum number of hits $N_{\text{hits,min}}$, and which lie within a distance, d, lateral to the bin with the highest number of entries. We chose $d = 10$ macro-pixels (≈ 1.1 cm) and $N_{\text{hits,min}} = 4$. The shower center (x_0, y_0) is calculated event-by-event, and the final distribution, $\mathrm{d}N_{\text{hits}}/\mathrm{d}x(x)$ is filled with pixel hits integrated in a range $|y_i - y_0| < 0.5$ mm. Since this method for the determination of the shower center depends on the number of pixel hits (not particle hits), the more realistic pixel response to particle hits in the Geant4 simulation is used, which is introduced in section 5.4. From simulation, we derive an uncertainty in the determination of $\sigma_{x_0} \approx 0.3$ mm with respect to the impact position of the electron, which is in the order of the standard deviation of a uniform probability distribution in the chosen bin width (i.e. $1.1\,\text{mm}/\sqrt{12} = 0.3\,\text{mm}$).

Figure 32 shows the measured and simulated transverse shower profiles in layers 5 and 10. The distributions are characterized by a sharp peak in the center (*core*) and exhibit broader side bands (*tails*). As a first-order estimate on which scale a discrimination against another nearby shower should be generally

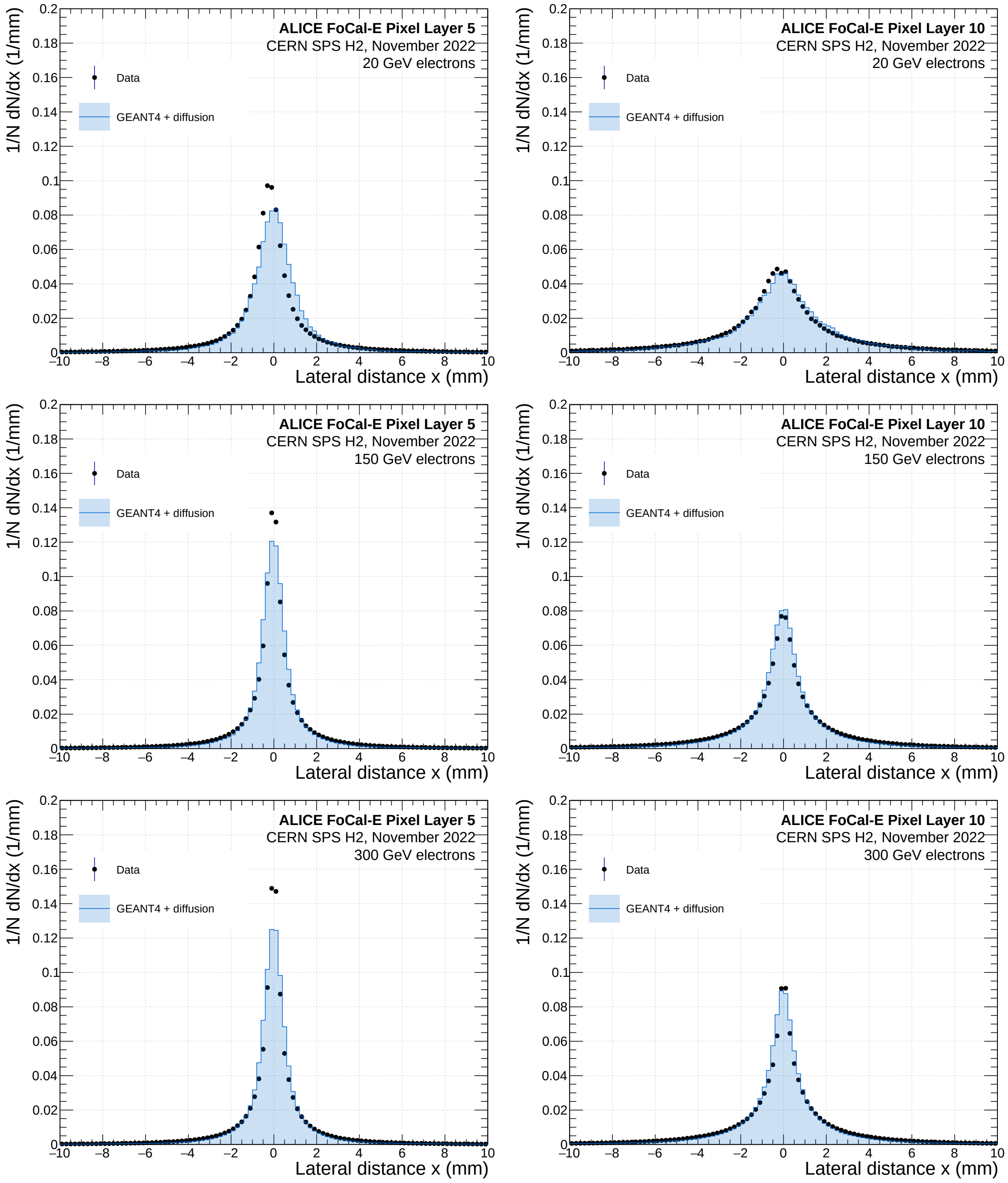

Figure 32. Measured and simulated lateral shower profiles for pixel layer 5 (left panels) and 10 (right panels) for 20, 150 and 300 GeV electrons. The bin width is 200 µm.

possible, we evaluate the Full Width Half Maximum (FWHM) of the measured distributions by finding the maximum bin, and the bin position where the distributions drop below the half of this maximum. Figure 33 shows the FWHM for layer 5 and 10, compared to simulations as a function of electron energy. From the resulting distributions we obtain an FWHM of 1.2 mm for electron energies of 20 GeV, and the FWHM drop with increasing energies down to 0.8 mm for electron energies of 300 GeV. The FWHM values are significantly smaller in layer 5 than in layer 10, which is expected because of the larger

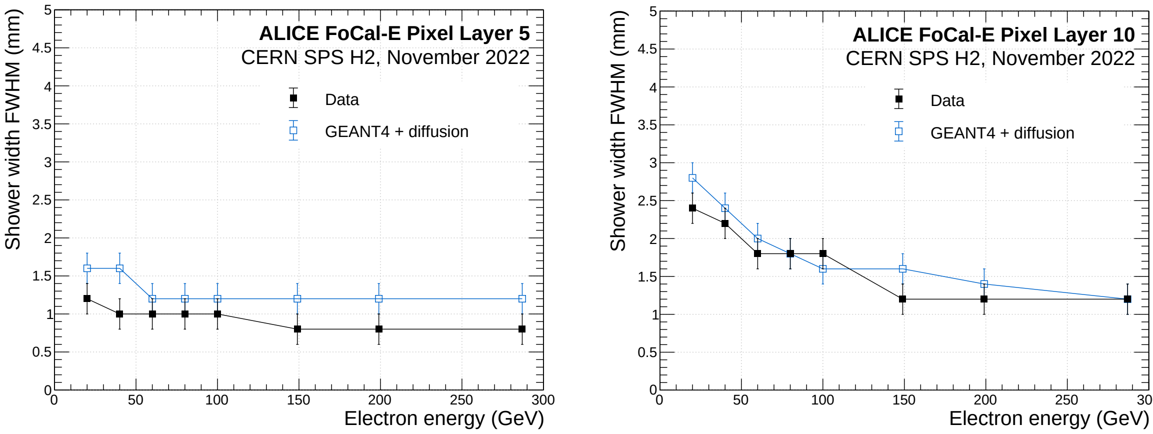

Figure 33. Measured and simulated FWHM for layer 5 (left panel) and 10 (right panel) versus electron energy. The error bars represent an uncertainty of 0.2 mm.

transverse spread at higher shower depths. In layer 10 the FWHM values for higher energy electrons are measured to be in the order of ≈ 1.2 mm, which is up to a factor of 2 higher than in layer 5, and the FWHM values increase towards lower electron energies, reaching 2.5 mm at 20 GeV. The simulation dataset — after having applied the cluster generation model — was analyzed with the same criteria for the determination of the shower center like the data. We compare the measured values to the simulated FWHM values with the diffusion model (introduced in section 5.4) applied. These values in layer 10 are in good agreement with the data in layer 10, but systematically higher than the data in layer 5. However, the measured and simulated FWHM of the transverse shower widths are in general consistent within ≈ 0.5 mm or better. The small discrepancies between data and simulation in layer 5 will be subject to further studies.

The analysis presented above is sensitive to the method of how the shower center is determined. However, it produces stable results in the full electron energy range tested in beam. For the higher energies a finer binning in the initial hitmap could be used in order to improve the determination of the shower center and thus the resolution of the shower width. However at lower energies where the hit density in the shower is lower, our method breaks down if the bin width is decreased to or below the scale of the hit density. Other experiments (e.g. [7]) have circumvented the uncertainty on the determination of the exact shower location by making an independent position measurement of the incident electron before it enters the calorimeter.

6 FoCal-H results

To study the FoCal-H response to high energy electrons and hadrons, dedicated standalone runs were performed with the same setup as shown in figure 12, but without FoCal-E in front of FoCal-H. In this way we isolate the performance of FoCal-H and avoid events in which a shower starts in the volume of FoCal-E. The data used to demonstrate the detector performance were recorded at the SPS H2 beam line in May, 2023. The hadron energies range from 60 to 350 GeV and are known to a relative precision of about 2% [37]. FoCal-H was rotated by 1 degree with respect to the beam direction to avoid particles directly hitting the fibers. A rotation by the same angle, which corresponds to $\eta \approx 5.3$ for particles originating from the nominal interaction point of ALICE, was also implemented in the respective simulations.

6.1 Data processing, pedestal determination and LG-HG matching

The CAEN DT5202 enables the user to set an individual bias voltage for each of the SiPMs of the detector. To equalize the SiPM overvoltage and thus the gain, a dedicated measurement of the breakdown voltage, V_{br}, was performed for each of the 249 SiPMs prior to the test beam campaign, as described in appendix B. The nominal operation voltage for each channel was chosen as $U = V_{br} + 3$ V. Each readout channel of the CAEN DT5202 has independent High Gain (HG) and Low Gain (LG) signal processing chains. The gains are programmable through variable-gain pre-amplifiers to provide a broad dynamic range. In this study, we use the suitably-scaled LG value to replace the HG value for events in which the HG ADC is above a given threshold, as described below. There is also the possibility of using time-over-threshold to determine the charge from a SiPM, but we have not employed this functionality of the DT5202.

For the presented results, the measure of the energy of an event is the sum of the ADC values of all channels firing in that event. The position of the FoCal-H prototype was adjusted remotely such that the beam spot was approximately in the geometric center of the front face of the detector. The low beam rate ensured that the probability of having more than one particle in the readout window of a given event was small, thus no clustering or other event selection was performed.

The CAEN software assumes a pedestal value of 25 ADC counts and any channel with an ADC value below this threshold is considered to be zero. However, this is not the actual pedestal value, which we determine for each of the 249 instrumented channels by summing all events for each channel for a given run, for both the HG and LG data. In order to estimate the mean position of the pedestal, the peak at low ADC values is fit with a Gaussian, whose mean defines the pedestal value. The pedestal is then subtracted from the ADC value for each channel for each event to give the pedestal subtracted ADC values. This procedure was carried out for both the HG and LG distributions.

To account for the saturation in the HG ADC values, above a certain HG ADC threshold the stored LG ADC values were used and scaled according to the following procedure. For each individual channel a correlation plot of the LG ADC versus the HG ADC was made.

The LG-HG correlation shows a region of linearity which was used to determine the gain ratio between the HG and LG signals. For each channel, the LG-HG correlation was fit using a first order polynomial to estimate this relative gain. The average slope for the 249 channels, reflecting the gain ratio between the HG and the LG, was found to be 9.3 with a spread of 0.2. We note that while, in principle, this parameter is derivable from the gain settings of the HG and LG amplifiers, minor differences in the capacitance values from channel to channel, presumably ascribable to the tolerances on the individual circuit components, cause the channel-to-channel variations. In the presented case, the obtained spread of 0.2 translates to about 2% channel-to-channel variations. The resulting fit parameters were used to correct the LG gain so that in cases where the HG is above a given threshold. For the presented results we used a value of 1500 for the HG-LG gain ratio, but the results were found to be insensitive to the exact value, as detailed below.

6.2 Calibration and linearity

For each beam energy, the ADC sum distribution was fit using a Gaussian fit function. The mean values of these fits were used to characterize the detector response for each beam energy and the values obtained are plotted as a function of the beam energy in figure 34. For the simulation, the number of photo-electrons was scaled by 1/3 to convert into ADC units.

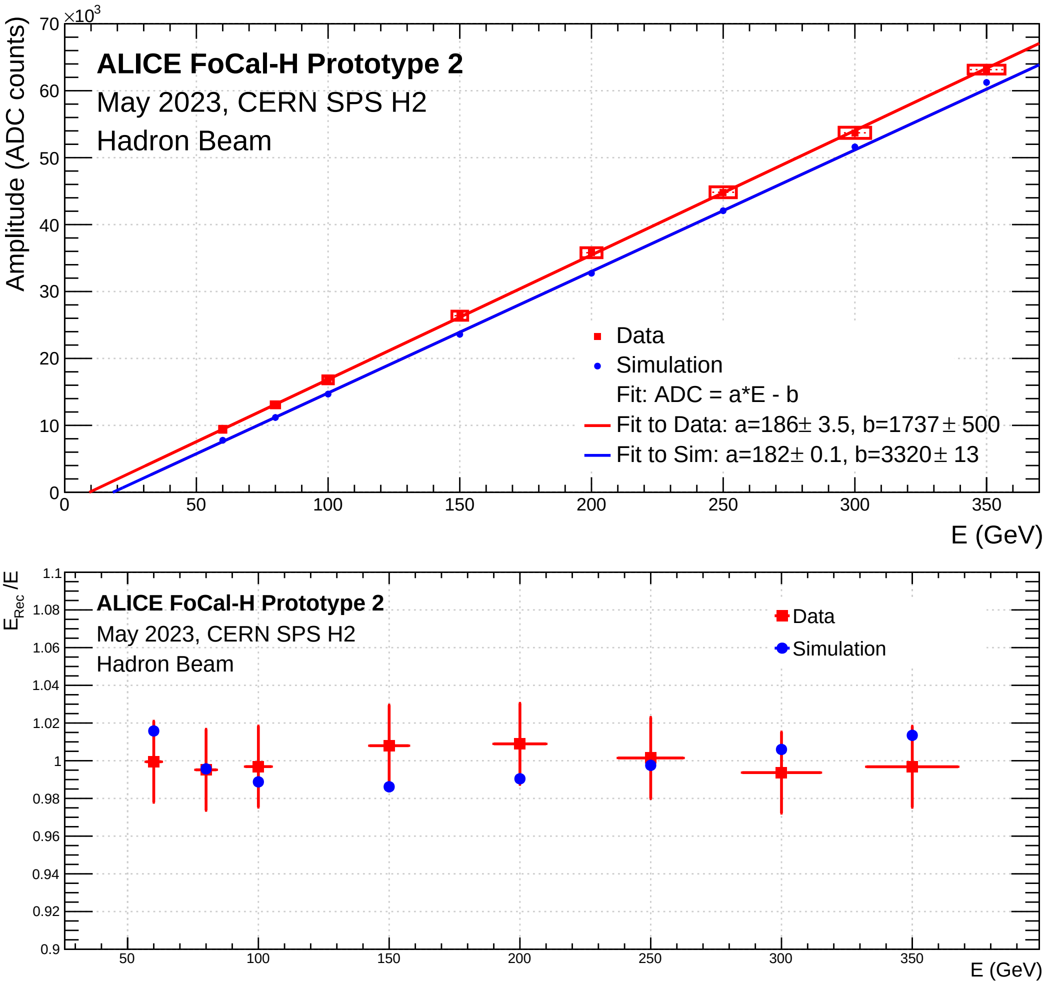

Figure 34. Top: foCal-H Prototype 2 reconstructed ADC sum for 60–350 GeV hadrons obtained at the H2 SPS beam line in May, 2023. The reconstructed ADC sum for the data is compared to simulations (where the number of photo-electrons was scaled by 1/3 to convert into ADC units). In each case, the dependence of the detector response is fitted with a linear function. Bottom: corresponding ratios between the reconstructed energy in the FoCal-H prototype and the beam energy.

The points were fitted with a linear function to obtain a relation between the ADC value and beam energy, as ADC = $a \times E - b$. The detector response from ADC channels to energy is obtained using this calibration function. As shown in figure 34, this was done separately for data and simulations. While the slopes of the fits in data and simulations are consistent within the uncertainties, the corresponding intercepts are not. The ratio between reconstructed energy and the beam energy, assumed to be the impinging particles energy, for both data and MC is shown in the bottom panel of figure 34. The uncertainty of the fit parameters is taken into account. The slope term dominates the 2% uncertainty. The beam energy uncertainty of 5%, entering through the denominator, is not included in the presented uncertainties. The nonlinearity is within the 2% range for the entire interval of hadron energy from 60 GeV to 350 GeV.

The detector simulations were performed as described in section 3. Three different hadron types were simulated: p, π^+, K^+. A weighted sum of the resulting distributions with weights

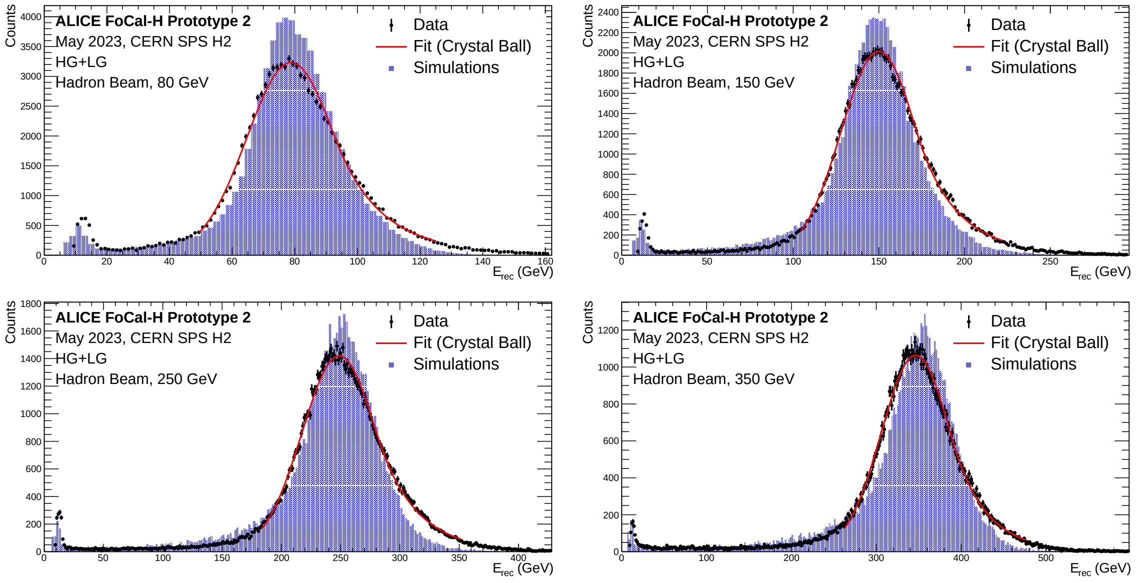

Figure 35. FoCal-H Prototype 2 reconstructed energy distributions for data and simulations for hadron energies at 80, 150, 250, and 350 GeV. The distributions are normalized to the same total number of events.

from the Atherton parametrisation [38] was made to properly reflect the composition of the SPS hadron beam at each energy. An additional correction for the decay probability of each particle between the production target and the FoCal-H prototype, located about 600 m downstream, was applied. An additional threshold was implemented for each channel in the simulations to mimic the pedestal subtraction in the data.

After applying the calibration, the measured and simulated response of FoCal-H to 80, 150, 250, and 350 GeV hadrons are shown in figure 35. At 60 GeV, pions comprise approximately 75% of the hadrons in the beam, while at 350 GeV there are almost exclusively protons. In all cases, the data exhibit broader tails than the simulation, with the difference decreasing with increasing hadron energy. An indication of the quality of the calibration is that the left peak in all of the reconstructed signal responses in data and simulations appears at the same energy.

6.3 Energy resolution

For each beam energy, the ADC sum distribution, calibrated as described above, was used. The distributions were fit using two different fitting functions — a Gaussian fit function and a Crystal Ball [39] fit function. These fit functions were used individually to compute the energy resolution σ_E/E. A three step fit procedure was employed. Initially, a fit with a Gaussian function was performed in the whole range of the histogram of the distribution. The mean and σ values were extracted providing the peak position. The second step was to fit in a selected range around the determined mean position from the first step. The final step was to re-fit within the given $n\sigma$ range, where the default range is given by $n = 2$, around the mean position from the second step, using either a Crystal Ball fit or a Gaussian fit. The results for the parameters of the different fit functions and ranges were used to calculate the systematic uncertainties of the fit. For each energy, the value of the FWHM of the peak was computed from the fit function and divided by 2.355 to extract σ_E/E, where E is the mean value of the final Gaussian fitting, described above.

2024 JINST 19 P07006

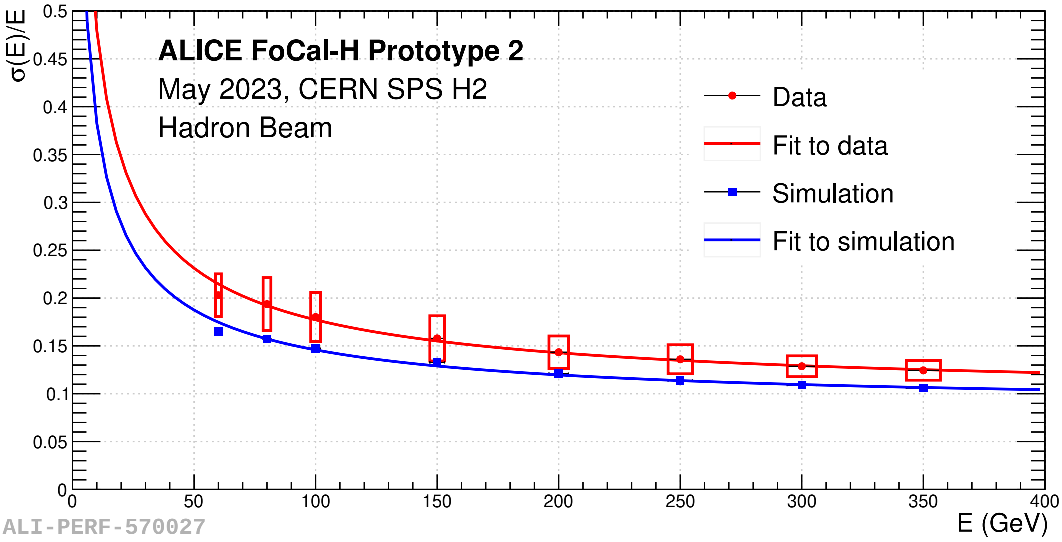

Figure 36. Energy resolution (obtained from FWHM/2.355) of the FoCal-H prototype 2 as a function of the hadron beam energy. The energy dependence was approximated using eq. (5.5). The corresponding fit values are: $\sigma_{\text{stoch.}} = 1.48$, $\sigma_{\text{noise}} = 0$, $\sigma_{\text{const.}} = 0.10$ for data, and $\sigma_{\text{stoch.}} = 1.18$, $\sigma_{\text{noise.}} = 0$, $\sigma_{\text{const.}} = 0.09$ for simulation.

The same procedure was applied both for data and simulations. The obtained resolution (σ_E/E) as a function of the impinging particle energy is shown in figure 36. As can be seen, the energy resolution in the simulations is significantly lower than the energy resolution observed in data. To account for this difference, a decrease of the number of the photoelectrons by more than factor 100 would have to be implemented. However, such large photon loss was considered not to be physical. The physics list applied in the simulation is, as mentioned in section 3, the QGSP_BERT. The usage of FTFP_BERT physics list in simulation (not shown) would result in an increase of the discrepancy between data and MC by 20%. Additional source of the discrepancy could be the spread of the channel by channel light collection efficiency, which was not accounted for in the simulation. The energy resolution was fitted using eq. (5.5), where we denote in the following $\sigma_{\text{stoch.}}$ as the stochastic, σ_{noise} the noise and $\sigma_{\text{const.}}$ the constant term. To estimate the systematic uncertainty, several effects were considered, most of which were studied for each beam energy and the total systematic uncertainty for each energy is shown with boxes in figure 36. However, being highly correlated, the systematic uncertainties of the individual data points were not used in the fit to the data. Instead, fits were performed independently for a given systematic variation (e.g. of the line shape assumptions), and the systematic uncertainty of the resolution parameters was obtained from all the different fits. In all cases, first the linearity was established (the resulting variation in the data is also shown in figure 34).

The systematic error arising from different fit ranges was studied by varying the limits of the right tail using a Crystal Ball fit for 1σ, 1.5σ, 2σ, 2.5σ. The maximal difference was taken to be the systematic error and amounts to $\Delta\sigma_{\text{stoch.}} = 0.02$, $\Delta\sigma_{\text{const.}} = 0.001$. The effect of the line shape was addressed by considering Gaussian and Crystal Ball fits. Their contribution to the systematic error is given by $\Delta\sigma_{\text{stoch.}} = 0.10$, $\Delta\sigma_{\text{const.}} = 0.005$. The effect of applying a different HG ADC threshold, at which the HG-LG method is applied was studied. The threshold at which the LG ADC was used rather than the HG ADC was varied by 500 to 4000 HG ADC counts, to investigate the impact of this threshold on the final result. The maximal difference was taken as systematic uncertainty and amounts to $\Delta\sigma_{\text{stoch.}} = 0.046$, $\Delta\sigma_{\text{const.}} = 0.003$. The maximal difference between the fit results using LG only and the HG-LG matching method gives a systematic uncertainty of $\Delta\sigma_{\text{stoch.}} = 0.20$, $\Delta\sigma_{\text{const.}} = 0.002$. The maximum $\Delta p/p$ of the H2 SPS beam line is 2% [37], used as the uncertainty on the beam energy (e.g. in figure 34), leading to a difference of $\Delta\sigma_{\text{stoch.}} = 0.04$ and $\Delta\sigma_{\text{const.}} = 0.003$. The noise term, denoted as σ_{noise}, is consistent with zero in all of the above studies. The relative systematic uncertainties due to the described effects are summarized in table 7.

Table 7. Estimation of the dominant systematic uncertainties (given in absolute values) on the stochastic and the constant term in the energy resolution parametrization of the FoCal-H prototype.

Systematic effect	$\Delta\sigma_{\text{stoch.}}$	$\Delta\sigma_{\text{const.}}$
Fit range	0.02	0.001
Line shape	0.10	0.005
HG-LG matching	0.05	0.003
Gain choice	0.20	0.002
Global energy scale	0.04	0.003
Total (added in quadrature)	0.22	0.007

Additional systematic effects such as the pedestal determination and beam composition were found to have negligible influence on the results. The final results for the energy resolution parameters are

$$\sigma_{\text{stoch.}} = (148 \pm 2_{\text{stat}} \pm 22_{\text{syst}})\%$$
$$\sigma_{\text{const.}} = (10.0 \pm 0.13_{\text{stat}} \pm 0.7_{\text{syst}})\%,$$

with the noise term consistent with zero. The uncertainty in these parameters is dominated by the systematic effects. The energy resolution of the FoCal-H prototype at high energy is dominated by the constant term and is of the order of 10%. This value is consistent with the expected performance of FoCal-H at high energies, and it is in line with the physics requirements, thus validating the chosen detector technology.

7 Summary

We constructed a full-length prototype of the FoCal, which is being developed for installation at LHC, CERN, and to take data in Run 4, starting from 2029. The final detector is designed to cover a pseudorapidity acceptance between 3.2 and 5.8 units and provide unique capabilities in probing non-linear QCD dynamics in unexplored regions at low Bjorken x and Q^2. The detector is composed of a silicon-tungsten electromagnetic sampling calorimeter with 20 layers (FoCal-E) and a hadronic calorimeter (FoCal-H) in spaghetti design with copper tubes. In FoCal-E, 18 sampling layers are equipped with silicon pad sensors of pad sizes of $1 \times 1\,\text{cm}^2$ and read out with the HGCROC, and two layers at position 5 and 10 are instrumented with ALPIDE chips with a pixel size of about $30 \times 30\,\mu\text{m}^2$. The copper tubes in FoCal-H of an outer (inner) diameter of 2.5 (1.2) mm are filled with scintillating fibers which are connected and read out with SiPMs at the rear detector side. The data were taken in various test beam campaigns between 2021 and 2023 at the CERN PS and SPS beam lines with hadron beams up to energies of 350 GeV, and electron beams up to 300 GeV.

Regarding the FoCal-E pad sensors, a comprehensive study of the response to MIPs across all pad layers was presented, revealing very clean signals and good stability over various hadron energies recorded (figure 19). Good agreement between data and simulations for longitudinal shower profiles for 20–300 GeV electrons was demonstrated (figure 26). Correspondingly, the linearity of the response was found to be in good agreement between data and simulations over the full range of available electron energies (figure 28). The relative energy resolution was found to be lower than 3% at energies larger than 100 GeV (figure 29), and projections using data up to 300 GeV with 17 functional pad-layers demonstrate that the energy resolution fulfills the requirements for the physics needs. Due to the high granularity and good linearity of the pixel layers (left panel of figure 25), measured transverse shower widths, quantified by FWHM, on the scale of mm were obtained, with good agreement to simulations (figure 33). The response of FoCal-H was found to be linear (figure 34), albeit with a significant intercept that is about factor 2 larger than in simulations. The shape of the response is non-Gaussian, with wider tails in the data as in simulations (figure 35). The corresponding resolution was quantified using the FWHM and decreases from about 16% at 100 GeV to about 11% at 350 GeV. The constant term of the resolution was estimated to be 10%, satisfying the physics needs.

Initial analyses on combining the FoCal-E with FoCal-H information show promising results e.g. for hadronic showers starting in FoCal-E, despite the use of the different DAQ systems. However, results of those studies are deferred to future publications.

Acknowledgments

We would like to express our most sincere gratitude to the collaborating individuals, groups, and organizations for their invaluable contributions to the success of the test beam campaigns mentioned in this document. We value the contribution of the ALICE FLP team providing us with the CRU and FLP. In particular, we warmly thank F. Costa, and R. Divia for their support with the O2 online infrastructure. We value the contribution of the ALICE CTP group for providing the LTU and their support on the trigger hardware and processing. In particular, we warmly thank A. Jusko, M .Krivda and R. Lietava for their kind help in developing and operating the FoCal trigger system. We are also very grateful for the support of the ALICE ITS team, and in particular S. Beole, O. Grøttvik and F. Reidt, for providing the necessary hardware and expertise for the design and development of the HIC-based high-granularity layers, and their readout infrastructure. Finally, we deeply appreciate the invaluable help of C. De la Taille and the OMEGA group in the development and understanding of the HGCROC chip based readout employed for the silicon pads sensors of FoCal. We extend our appreciation to the staff and operators of the PS and SPS test beam facilities at CERN for their assistance in setting up and conducting the experiment operations. In particular, we would like to mention D. Banerjee, N. Charitonidis, B. Holzer, M. Lazzaroni and B. Rae. Their expertise and endless support ensured a smooth and productive data-taking process.

I. Bearden, A. Buhl, L. Dufke and I. Pascal acknowledge support from the The Carlsberg Foundation (CF21-0606) and the Danish Council for Independent Research/Natural Sciences. M. Bregant acknowledges financial support by Conselho Nacional de Desenvolvimento Científico e Tecnológico (CNPq) and Fundação de Amparo à Pesquisa do Estado de São Paulo (FAPESP) grant No. 2020/04867-2, Brazil. T. Chujo, Y. Goto, and T. Sugitate acknowledge the support by JSPS KAKENHI Grant

Numbers JP20H05638, JP19H01928, JP21H04484. A. Gautam, T. Isidori and D. Tapia Takaki are supported by the U.S. Department of Energy, Office of Science, Office of Nuclear Physics under award number: DE-SC0020914. V. Kozhuharov and R. Simeonov acknowledge that partially this study is financed by the European Union-NextGenerationEU, through the National Recovery and Resilience Plan of the Republic of Bulgaria, project SUMMIT BG-RRP-2.004-0008-C01. N. Minafra and D. Tapia Takaki acknowledge support by the U.S Department of Energy, Office of Science, Office of Basic Energy Sciences, under Award Number: DE-SC0023510. H. Hassan, L.M.Huhta, Y. Melikyan, S.S. Räsänen and H. Rytkönen acknowledge financial support from the Helsinki Institute of Physics (HIP), Finland and the Academy of Finland (Center of Excellence in Quark Matter) (grant nos. 346327, 346328), Finland. M. Fasel, F. Jonas, C. Loizides and N. Novitzky acknowledge financial support by the U.S. Department of Energy, Office of Science, Office of Nuclear Physics, under contract number DE-AC05-00OR22725. L. He, J. Yi, Z. Yin and D. Zhou acknowledge the support by the National Key Research and Development Program of China (2022YFA1602103). Researchers from Norwegian institutes acknowledge the support by the The Research Council of Norway, Norway.

A Calibration of the FoCal-E pads

This section provides further details to the calibration procedure for the HGCROC which was introduced in section 5.5 and used for the electron data analysis described in sections 5.6 to 5.8. The calibration pulser supports two charge injection regimes: one for low-range injection with an 0.5 pF capacitor, $C_{\text{inj,low}}$, and one for high-range injection with an 8.0 pF capacitor, $C_{\text{inj,high}}$. An integrated 11-bit Digital-to-Analog Converter (DAC), DAC_{inj}, allows to set the voltage at the injection capacitors, up to the chip's bandgap voltage of 1 V. Thus, two charge injection regimes with a range of 0.5 pC and 8.0 pC, respectively, are supported. The injected charge, Q_{inj}, is obtained from the product of the size of the injection capacitor, the voltage fraction set in DAC units, and the HGCROC's band-gap voltage reference:

$$Q_{\text{inj}} = C_{\text{inj}} \times \frac{\text{DAC}_{\text{inj}}}{2048} \times U_{\text{ref,bandgap}} \,. \tag{A.1}$$

The UDP operation mode of the aggregator board described in section 2.1 was used to run and record the calibration of the channel-wise ADC, ToA, and ToT response. A dedicated DAQ software controls the chip internal injection system through the slow control link. For injection, the pulse injection command is fired through the FCMD port, and it simulates the signal of the Si pads sensors in each layer [16]. Among the set of options, the calibration script includes the control over the number of injections and the granularity of the injection steps. For the calibration procedure, the voltage is incremented step-wise in steps of 10 DAC units starting from zero, and per step 2000 injections are released. The custom DAQ software records the per-channel response of ADC, ToT, and ToA per charge injection, and the mean response per step is calculated, as displayed in figure 37. The ToT and ToA units can be translated directly into the time-over-threshold and time-of-arrival of the charge pulse where 1 ToT unit = 50 ps, and 1 ToA unit = 25 ps. We optimized the threshold setting for ToA and ToT by performing a scan of their response as a function of the applied thresholds.

For that, a few parameters of the pre-amplifier of the HGCROC have to be previously adjusted for characterizing the gain of the chip and optimize the dynamic range of the readout circuit. In particular, a few combinations of feedback resistors and capacitors values can be explored modifying

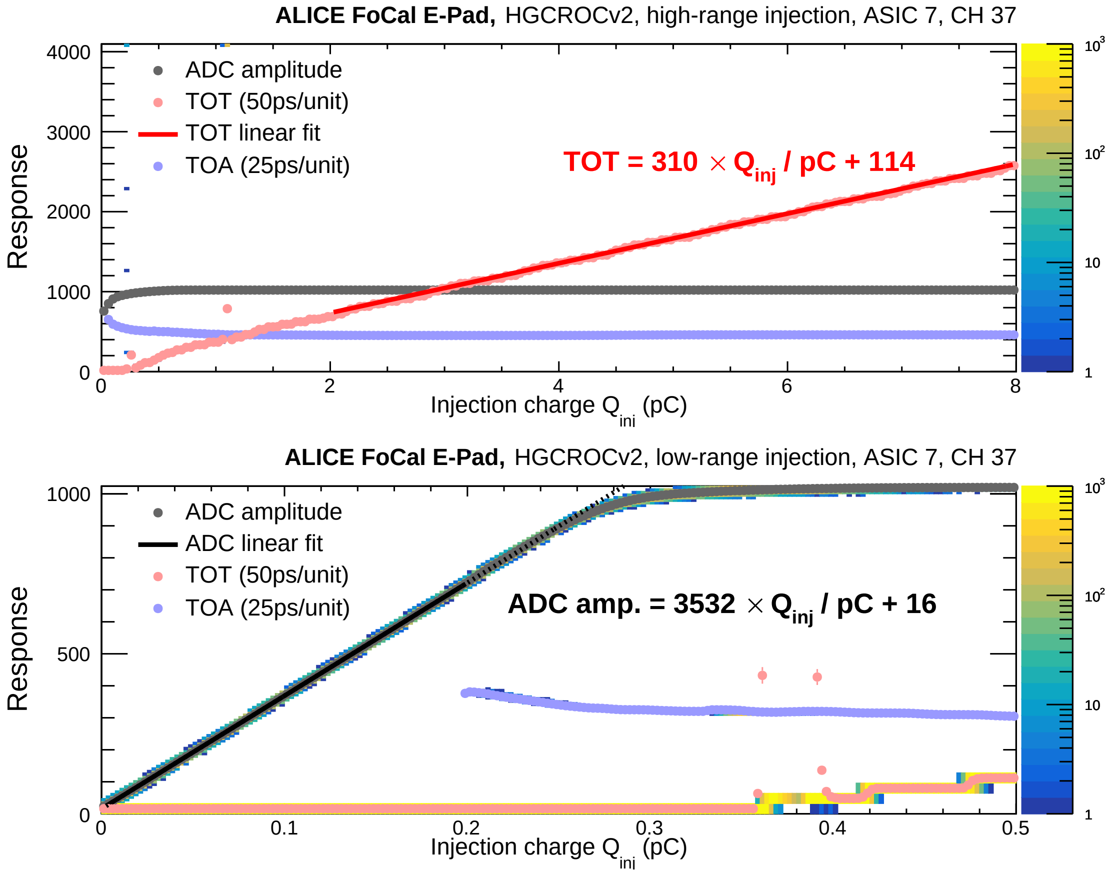

Figure 37. Top: response of the ADC, ToA, and ToT as a function of the injected charge for a single channel of ASIC 7. The calibration is operated over the full high-range injection range spanning from 0–8.0 pC. Bottom: the response for the low-range injection region going from 0–0.5 pC. The TOT response is fitted in the range from 2 to 8 pC in the high-range injection mode (top), and the ADC amplitude from 0 pC to 200 fC in the low-range injection mode (bottom).

the parameters of the configuration files in the acquisition software. The chip dynamic range and MIP response were initially tested at the PS test beam facility with a comprehensive scan of these pre-amplification parameters. Selected results are shown in section 5.1; details can be found in [32].

After introducing the use of the ADC phase selection through the trigger board (described in section 4), the optimal working point of the detector underwent slight modifications and the pre-amplification circuit needed additional tuning. The parameters selected for the FoCal-E 2023 data acquisitions were chosen to achieve the best compromise between a broad dynamic range, and optimal MIP separation in the ToT and ADC domains. The results relative to the 2023 MIP studies are reported in section 5.1, and an example is provided in figure 19. The total HGCROC pre-amplifier feedback resistance is defined by the parallel of two resistors. Similarly, the total capacitance is obtained by the parallel of the two feedback capacitors. The values set for the FoCal-E setup are:

- $R_F = 100\,\mathrm{k\Omega} \parallel 66\,\mathrm{k\Omega} = 39.8\,\mathrm{k\Omega}$
- $C_f = 100\,\mathrm{fF} \parallel 400\,\mathrm{fF} = 500\,\mathrm{fF}$

2024 JINST 19 P07006

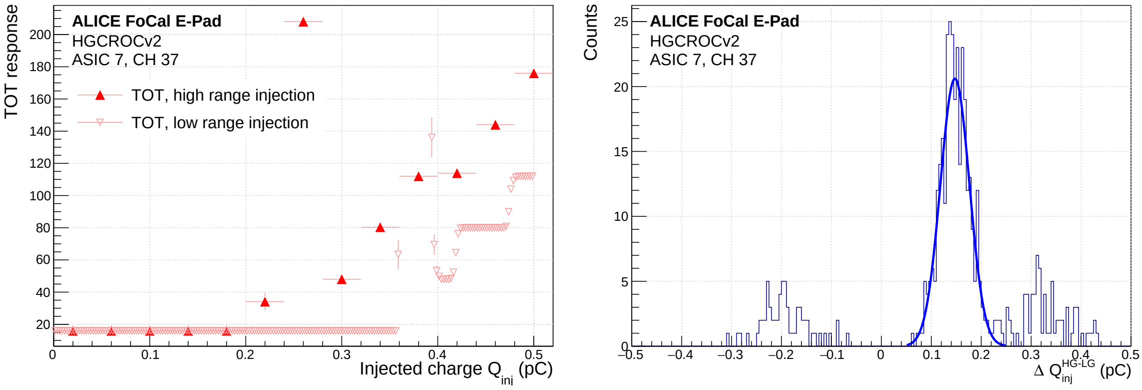

Figure 38. Left: ToT response as a function of the injected charge for high-range and low-range injection regimes. Right: the difference, $\Delta Q_{\text{inj}}^{\text{HG}-\text{LG}}$, of the ToT turn-on position between high-range and low-range injection, fitted with a Gaussian curve in order to extract the mean.

Once the circuit's gain was characterized, the best ToT and ToA thresholds were found to amount to, respectively, 300 and 400 units. These settings results in a gap of 100 fCbetween the dynamic range of the ADC and the turn-on region of the ToT. However, it significantly reduced the noise of ToT and ToA, leading to an overall more stable detector operation.

While the chip's performance shows a good linearity (about ± 0.1% of the full dynamic range) in the tests performed by the development team [16], a design error in the grounding routing of the ASIC produces an irreducible voltage offset, $\Delta U_0 = 30\,\text{mV}$, in the charge injection schematic. This effectively limits the minimum injection to about $\Delta Q_{\text{min}}^{\text{LG}} = 0.5\ \text{pF} \times 30\ \text{mV} = 15\,\text{fC}$. Similarly, this contribution results in an offset of $\Delta Q_{\text{max}}^{\text{HG}} = 8.0\ \text{pF} \times 30\ \text{mV} = 240\,\text{fC}$ in the high-range regime. This effect is shown in figure 38, where the ToT is reported as a function of the injected charge. For our detector, we determine ΔU_0 from data by evaluating per channel the discrepancy in the turn-on position of the ToT between low-range and high-range injection. A simple computer program was written which coarsely finds the position (expressed in units of charge according to eq. (A.1)) where the first ToT values > 0 are measured, as depicted in figure 38 (left). The distribution of evaluated offsets between the two ranges is shown in figure 38 (right). We evaluate an offset of $\Delta Q_{\text{inj}}^{\text{HG}-\text{LG}} = 150\,\text{fC}$ from a Gaussian fit to the main peak.

$$\Delta U_0 = \frac{\Delta Q_{\text{inj}}^{\text{HG}-\text{LG}}}{C_{\text{inj,high}} - C_{\text{inj,low}}} = \frac{150\,\text{fC}}{8.0\,\text{pF} - 0.5\,\text{pF}} = 20\,\text{mV}\,, \tag{A.2}$$

which is in reasonable agreement with the expectation of 30 mV. The channel-wise calibration parameters are obtained from linear fits in the domain $Q_{\text{inj}} < 0.2\,\text{pC}$ for the ADC, and $Q_{\text{inj}} > 2\,\text{pC}$ for ToT, as shown in figure 37. The calibrated ToT values are corrected by the constant charge offset ΔQ_{inj}. For lower charge values (in particular in the turn-on region), the response of the ToT is not linear, and we derive a calibration by linearly interpolating between the ToT response at 0 and 2 pC (where the former one is always zero). Figure 39 shows the distribution of the fitted slope parameters for the ADC amplitude (left panel) and the ToT response (right panel). The two populations in the histograms are most likely related to the slightly different architectures in the two halves of the HGCROC, and therefore to the ID of the front-end channels. For the ADC response we obtain from our calibration procedure a mean response factor of 3650 units/ pC = 3.65 units/ fC for channel IDs < 36 and

2024 JINST 19 P07006

3500 units/ pC = 3.50 units/ fC for channel IDs ≥ 36. In particular, the ADC response to a minimum ionizing particle is expected to be around 3.6 units/ fC · 3.7 fC = 13.3 units, where the MPV of 3.7 fC was used to describe the charge generated by a MIP in 300 µm silicon. The slope of the ToT response was calibrated to be 310 units/ pC and 305 units/ pC, respectively, and the ToT offset was in the order of 120 units (not shown). In channels where the high-range ToT calibration procedure failed, the mean values of the fitted parameters in the corresponding ASIC half were assigned. For the ADC only the proportionality factor was used for the calibration, and the channel-wise pedestal to subtract was determined from dedicated pedestal runs without beam signal. The successful calibrations were then used to convert the response of the HGCROC to actual charge deposit in the pad sensors components.

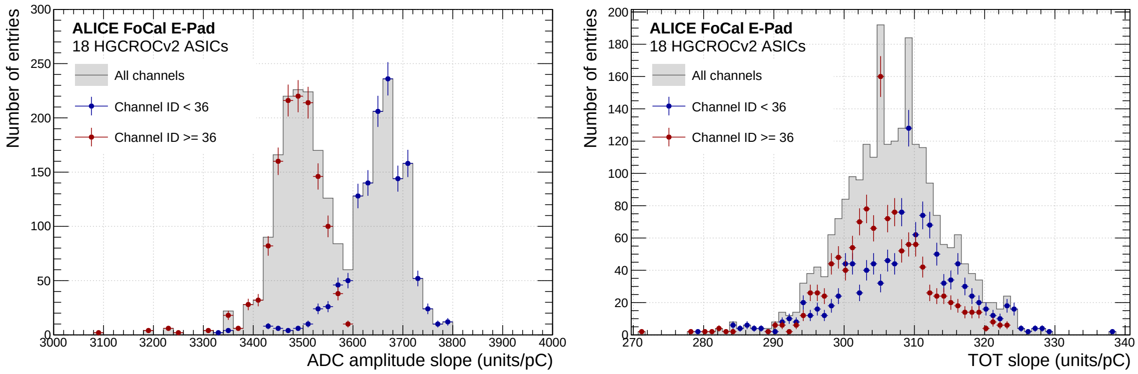

Figure 39. Fitted slope parameter for the calibration of ADC and ToT response. The two populations in the histograms are related to the slighlty different architectures in the two halves of the HGCROC.

B Inter-calibration of the SiPMs for FoCal-H

One of the main ingredients for the calibration of the FoCal-H is the gain (inter-)calibration of the SiPMs. The second prototype of FoCal-H uses 249 HPK S13360-6025 SiPMs. However, the manufacturer does not guarantee the equality of the breakdown voltage ($\mathrm{V_{br}}$), declaring it as 53 ± 5 V [40]. The CAEN DT5202 used to readout the towers allows one to bias SiPMs with individually-adjusted voltage values. To equalize their overvoltage and thus the SiPM gain, a dedicated measurement of $\mathrm{V_{br}}$ was performed for each photosensor prior to the test beam campaign.

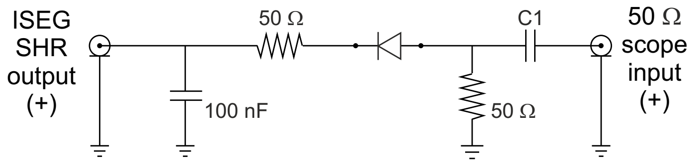

Figure 40. Circuitry of the SiPM bias and readout board used for the V_{br} measurement. Using $C1 = 1.5$ pF corresponds to the low-gain operation mode of the CAEN DT5202 system, $C1 = 15$ pF corresponds to the high-gain operation mode.

The large number of SiPMs used in the prototype, and ultimately in the future detector assembly, prioritized the choice of a simplified technique to determine $\mathrm{V_{br}}$. This was done by measuring the individual dependencies of bias current versus bias voltage (I-V curves). For this, each SiPM was

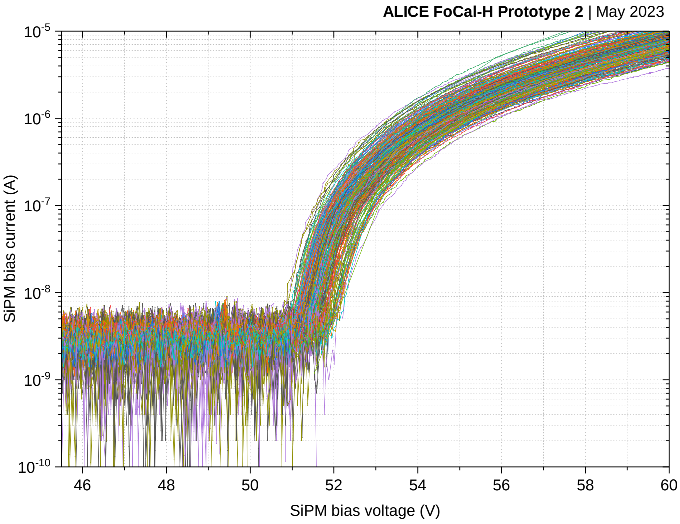

Figure 41. I-V curves measured for each SiPM at 0.1 V/s ramp rate.

connected according to the circuitry shown in figure 40, replicating the one used in the CAEN DT5202 modules [26]. The I-V curves were measured at a ramp-up rate of 0.1 V/s, which was low enough to keep the "background" current below 5 nA.

Figure 41 shows the 249 I-V curves measured for all SiPMs. To derive the precise point corresponding to the true V_{br} value, various techniques could be considered depending on the exact application [41]. For our application, the primary goal was the relative gain-matching of the 249 SiPMs. Therefore, as a simple technique consistent for all devices tested, V_{br} was defined as the point at which the current exceeds the 10 nA threshold.

Figure 42 (left) shows the resulting distribution of V_{br}, with mean of 51.5 V and a spread of 0.3 V. Another approach is to define the starting point of the exponential rise of the I-V curve above the breakdown voltage with an exponential fit. The average difference between this and the former approach is 0.43 V with a standard deviation of 0.05 V, as shown in the right panel of figure 42.

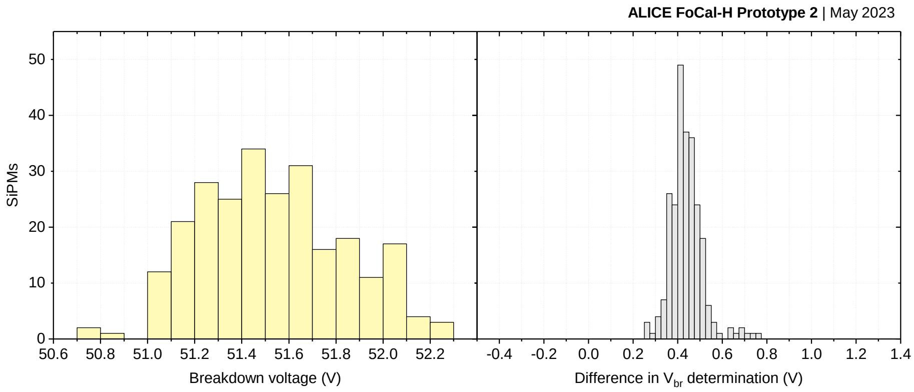

Figure 42. Left: spread of the V_{br} for the 249 SiPMs defined at the point where the current exceeds the 10 nA threshold; mean = 51.5 V, standard deviation = 0.3 V. Right: difference in V_{br} between the values determined by a simple threshold or by exponential fitting; mean = 0.43 V, standard deviation = 0.054 V.

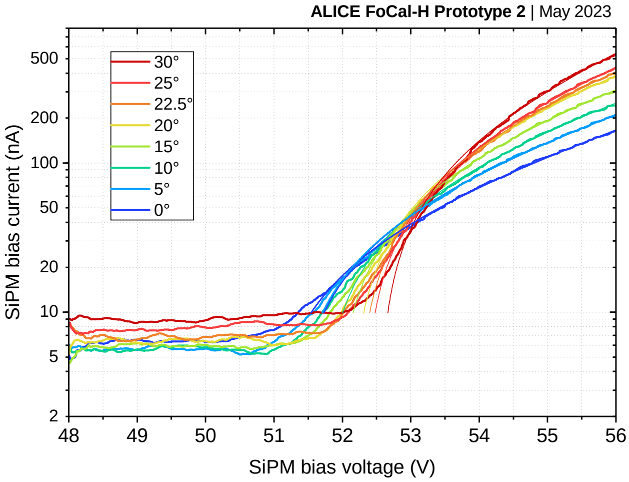

Figure 43. I-V dependence of one SiPM measured for various SiPM temperatures.

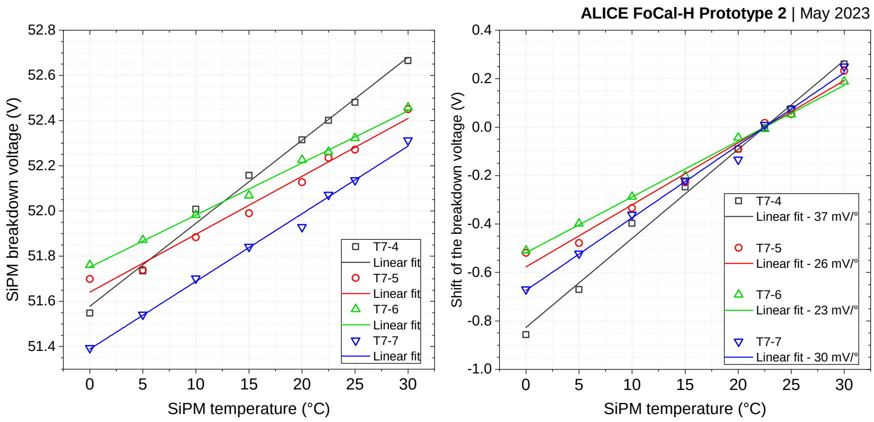

Figure 44. Left: breakdown voltages of the four SiPM (named T7-4 to T7-7) on the test board as a function of temperature. Right: shift of the breakdown voltages of the four SiPMs on the test board as a function of temperature.

The light-tight box used as the SiPM test bench was not thermostabilized, but the temperature in the SiPM vicinity was monitored with a probe. The entire characterization process was conducted at 22 ± 0.6°C. Influence of such temperature spread to the precision of the V_{br} was estimated by characterizing the behavior of four SiPMs on a test board in a climatic chamber. Figure 43 shows the I-V temperature dependence for one of the SiPM. Figure 44 summarizes the temperature dependence of the breakdown voltage (left) and the difference to the nominal breakdown voltage (right) for each of the 4 SiPMs. A typical temperature coefficient of V_{br} is 29 mV/K was found. Although there is a significant spread of 25% (at a fairly small statistics of 4 devices), we estimate minor temperature variations of the SiPMs in the test board to result in an uncertainty below ±10 mV.

The inherent spread in $\mathrm{V_{br}}$ seen at the statistics of 249 SiPMs (±0.6 V) results in ±20% spread in gain and ±15% spread in PDE at 3V overvoltage [40]. The outcome of the gain-matching, as measured for the limited set of 7 SiPMs of a test board under a uniform illumination with 440 nm light, was a ±3.7% spread in the response function, as shown in figure 45.

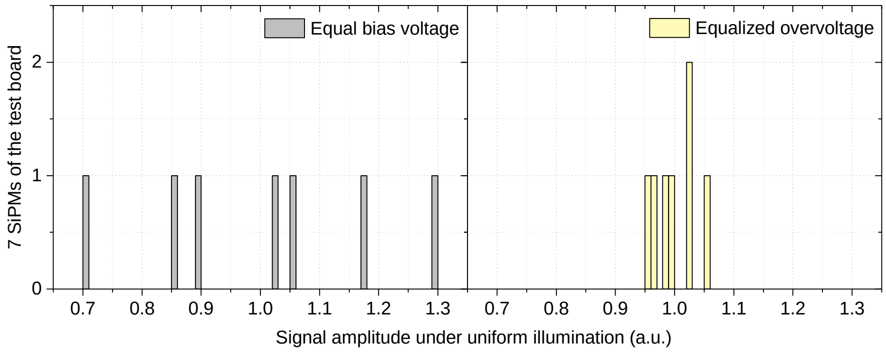

Figure 45. Response function (gain × Photon Detection Efficiency (PDE)) of the 7 SiPMs of the test board under a uniform 440 nm illumination. Left: measured at equal bias voltage with an average overvoltage of 3 V; standard deviation: 20%. Right: measured at equal overvoltage; standard deviation: 3.7%.

Acronyms

ADC Analog-to-Digital Converter.

ALICE A Large Ion Collider Experiment.

ALPIDE ALICE PIxel DEtector.

ASIC Application-Specific Integrated Circuit.

BERT Bertini Cascade Model.

CERN Conseil Européen pour la Recherche Nucléaire.

CMN Common Mode Noise.

CMOS Complementary Metal Oxide Semiconductor.

CMS Compact Muon Solenoid.

COTS Commercial Off-The-Shelf.

CRU Common Readout Unit.

CTP Central Trigger Processor.

DAC Digital-to-Analog Converter.

DAQ Data Acquisition.

EM Electromagnetic.

FCMD Fast Command.

FF FireFly.

FIFO First In First Out.

FLP First Level Processor.

FoCal Forward Calorimeter.

FoCal-E Electromagnetic Forward Calorimeter.

FoCal-H Hadronic Forward Calorimeter.

FPC Flexible Printed Circuit.

FPGA Field-Programmable Gate Array.

FR4 Flame Retardant.

FTFP FriTioF parton model and Precompound model.

FWHM Full Width Half Maximum.

GBT GigaBit Transceiver.

HG High Gain.

HGCal High Granularity Calorimeter.

HGCROC High Granularity Circuit ReadOut Chip.

HIC Hybrid Integrated Circuit.

HPK Hamamatsu Photonics K.K..

IB Inner Barrel.

IP Internet Protocol.

ITS Inner Tracking System.

langaus A convoluted Landau and Gaussian distribution implemented in ROOT.

LDO Low-DropOut.

LG Low Gain.

LHC Large Hadron Collider.

LTU Local Trigger Unit.

MAPS Monolithic Active Pixel Sensor.

MC Monte Carlo.

MIP Minimum Ionizing Particle.

MPV Most Probable Value.

O2 ALICE Online–Offline Computing System.

OB Outer Barrel.

OMEGA Organization for Micro-Electronics desiGn and Applications.

PCB Printed Circuit Board.

pCT proton Computed Tomography.

PDE Photon Detection Efficiency.

PLL Phase Locked Loop.

PS Proton Synchrotron.

QC Quality Control.

QGSP Quark-Gluon String model and Precompound model.

ROOT ROOT — An Object-Oriented Data Analysis Framework.

RU Readout Units.

SFP Small Form-factor Pluggable.

SiPM Silicon Photomultiplier.

SNR Signal-to-Noise Ratio.

SoC System-on-Chip.

SPS Super Proton Synchrotron.

SpTAB Single point TAB.

TC Transition Card.

TCP Transmission Control Protocol.

TDC Time-to-Digital Converter.

TDR Technical Design Report.

TF Time Frame.

ToA Time-of-Arrival.

ToT Time-over-Threshold.

TTL Transistor-Transistor Logic.

UDP User Datagram Protocol.

ZIF Zero Insertion Force.

References

[1] ALICE collaboration, *Letter of Intent: A Forward Calorimeter (FoCal) in the ALICE experiment*, CERN-LHCC-2020-009 CERN, Geneva, Switzerland (2020).

[2] ALICE collaboration, *The ALICE experiment at the CERN LHC*, 2008 *JINST* **3** S08002.

[3] ALICE collaboration, *Physics of the ALICE Forward Calorimeter upgrade*, ALICE-PUBLIC-2023-001 CERN, Geneva, Switzerland (2023).

[4] ALICE collaboration, *Physics performance of the ALICE Forward Calorimeter upgrade*, ALICE-PUBLIC-2023-004 CERN, Geneva, Switzerland (2023).

[5] A.P. de Haas et al., *The FoCal prototype — an extremely fine-grained electromagnetic calorimeter using CMOS pixel sensors*, 2018 *JINST* **13** P01014 [`arXiv:1708.05164`].

[6] J. Alme et al., *Performance of the electromagnetic pixel calorimeter prototype Epical-2*, 2023 *JINST* **18** P01038 [`arXiv:2209.02511`].

[7] T. Peitzmann et al., *Results from the EPICAL-2 ultra-high granularity electromagnetic calorimeter prototype*, *Nucl. Instrum. Meth. A* **1045** (2023) 167539 [`arXiv:2207.01815`].

[8] S. Muhuri et al., *Test and characterization of a prototype silicon-tungsten electromagnetic calorimeter*, *Nucl. Instrum. Meth. A* **764** (2014) 24 [`arXiv:1407.5724`].

[9] S. Muhuri et al., *Fabrication and beam test of a silicon-tungsten electromagnetic calorimeter*, 2020 *JINST* **15** P03015 [`arXiv:1911.00743`].

[10] R.G.E. Barthel et al., *A Large-Scale Pad-Sensor Based Prototype of the Silicon Tungsten Electromagnetic Calorimeter for the Forward Direction in ALICE at LHC*, `arXiv:2306.06153`.

[11] T. Awes et al., *Design and performance of a silicon-tungsten calorimeter prototype module and the associated readout*, *Nucl. Instrum. Meth. A* **988** (2021) 164796 [`arXiv:1912.11115`].

[12] CALICE collaboration, *The CALICE SiW ECAL Technological Prototype — Status and Outlook*, *Instruments* **6** (2022) 75 [`arXiv:2211.07457`].

[13] CMS HGCAL collaboration, *Response of a CMS HGCAL silicon-pad electromagnetic calorimeter prototype to 20–300 GeV positrons*, 2022 *JINST* **17** P05022 [`arXiv:2111.06855`].

[14] A. Giaz et al., *Test beam results of the fiber-sampling dual-readout calorimeter*, *Nucl. Instrum. Meth. A* **1048** (2023) 167964.

[15] ALICE collaboration, *FoCal pad prototype and its test results*, 2020 *JINST* **15** C12003.

[16] CMS collaboration, *Performance study of HGCROC-v2: the front-end electronics for the CMS High Granularity Calorimeter*, 2020 *JINST* **15** C04055.

[17] O. Bourrion et al., *Prototype electronics for the silicon pad layers of the future Forward Calorimeter (FoCal) of the ALICE experiment at the LHC*, 2023 *JINST* **18** P04031 [`arXiv:2302.13912`].

[18] J.P. Cachemiche et al., *The PCIe-based readout system for the LHCb experiment*, 2016 *JINST* **11** P02013.

[19] P. Buncic, M. Krzewicki and P. Vande Vyvre, *Technical Design Report for the Upgrade of the Online-Offline Computing System*, CERN-LHCC-2015-006 CERN, Geneva, Switzerland (2015).

[20] ALICE collaboration, *Technical Design Report for the Upgrade of the ALICE Inner Tracking System*, *J. Phys. G* **41** (2014) 087002.

[21] S. Senyukov et al., *Charged particle detection performances of CMOS pixel sensors produced in a 0.18vm process with a high resistivity epitaxial layer*, *Nucl. Instrum. Meth. A* **730** (2013) 115 [`arXiv:1301.0515`].

[22] J. Alme et al., *A High-Granularity Digital Tracking Calorimeter Optimized for Proton CT*, *Front. Phys.* **8** (2020) 460.

[23] *Plastic Scintillating Fibers datasheet*, Tech. Rep., Saint-Gobain Ceramics & Plastics, Inc. (2021).

[24] *A1702/DT5702 32 Channel SiPM Readout Board for Cosmic Rays Veto*, Tech. Rep., CAEN SpA. (2023).

[25] ALICE collaboration, *Design and Test-Beam Results of the FoCal-H Demonstrator Prototype*, *Instruments* **6** (2022) 70 [`arXiv:2211.14791`].

[26] *CAEN A5202/DT5202 user manual*, Tech. Rep., CAEN SpA. (2023).

[27] *Citiroc 1A Scientific Instrumentation SiPM Read-Out Chip Data Sheet*, Tech. Rep., Weeroc (2021).

[28] *CAEN A5202/DT5202 Readout Software*, Tech. Rep., CAEN SpA. (2024).

[29] GEANT4 collaboration, *GEANT4–a simulation toolkit*, *Nucl. Instrum. Meth. A* **506** (2003) 250.

[30] GEANT4 collaboration, *Guide For Physics Lists, Release 10.6*, 6 December 2019.

[31] P. Buncic, M. Krzewicki and P. Vande Vyvre, *Technical Design Report for the Upgrade of the Online-Offline Computing System*, CERN-LHCC-2015-006 CERN, Geneva, Switzerland (2015).

[32] H.M. Rytkonen, *Simulated $\pi^0 - \pi^0$ Correlation and Test Beam Performance of the Future Forward Calorimeter in the ALICE experiment*, Ph.D. thesis, Jyväskylä University, Jyväskylä, Finland (2023).

[33] N. Akchurin, *Detailed results of the response of a CMS HGCAL silicon-pad electromagnetic calorimeter prototype to 20-300 GeV positrons*, CMS-NOTE-2021-009, CERN, Geneva, Switzerland (2021).

[34] H.E.S. Pettersen, *A Digital Tracking Calorimeter for proton Computed Tomography*, Ph.D. thesis, University of Bergen, Bergen, Norway (2018).

[35] H.E.S. Pettersen et al., *Proton tracking in a high-granularity Digital Tracking Calorimeter for proton CT purposes*, *Nucl. Instrum. Meth. A* **860** (2017) 51 [`arXiv:1611.02031`].

[36] PARTICLE DATA Group, *Review of Particle Physics*, *PTEP* **2022** (2022) 083C01.

[37] *The H2 Secondary Beam Line of EHN1/SPS*, Tech. Rep., CERN, Geneva, Swizerland (2017).

[38] H.W. Atherton et al., *Precise Measurements of Particle Production by 400-GeV/c Protons on Beryllium Targets*, CERN-80-07 CERN, Geneva, Switzerland (1980) [`DOI:10.5170/CERN-1980-007`].

[39] ALICE collaboration, *Quarkonium signal extraction in ALICE*, ALICE-PUBLIC-2015-006 CERN, Geneva, Switzerland (2015).

[40] *S13360 series MPPC datasheet*, Tech. Rep., HAMAMATSU Photonics K.K. (2022).

[41] F. Nagy, G. Hegyesi, G. Kalinka and J. Molnar, *A model based DC analysis of SiPM breakdown voltages*, *Nucl. Instrum. Meth. A* **849** (2017) 55 [`arXiv:1606.07805`].